addenda and errata

Diffraction with a coherent X-ray beam: dynamics and imaging. Erratum

Frédéric Livet

LTPCM-ENSEEG, UMR-CNRS 5614, INPG/UJF, BP 75, 38402 St Martin d'Hères, France. Correspondence e-mail: flivet@ltpcm.inpg.fr

In the paper by Livet [*Acta Cryst.* (2007), A**63**, 63–87], equation (15) is incorrect. The correct equation is

$$\beta(z) = \left\{ \sum_{n=0}^{\infty} (-1)^n 2^{2n+2} z^{2n} / [(2n+1)(2n+2)^2(2n+1)!] \right\}^2. \quad (15)$$

Diffraction with a coherent X-ray beam: dynamics and imaging

Frédéric Livet

LTPCM-ENSEEG, UMR-CNRS 5614, INPG/UJF, BP 75, 38402 St Martin d'Hères, France. Correspondence e-mail: flivet@ltpcm.inpg.fr

Methods for carrying out coherent X-ray scattering experiments are reviewed. The brilliance of the available synchrotron sources, the characteristics of the existing optics, the various ways of obtaining a beam of controlled coherence properties and the detectors used are summarized. Applications in the study of the dynamics of speckle patterns are described. In the case of soft condensed matter, the movement of inclusions like fillers in polymers or colloidal particles can be observed and these can reflect polymer or liquid-crystal fluctuations. In hard condensed-matter problems, like phase transitions, charge-density waves or phasons in quasicrystals, the study of speckle fluctuations provides new time-resolved methods. In the domain of lensless imaging, the coherent beam gives the modulus of the sample Fourier transform. If oversampling conditions are fulfilled, the phase can be obtained and the image in the direct space can be reconstructed. The forthcoming improvements of all these techniques are discussed.

1. Introduction

When X-rays are used in diffraction experiments, it is necessary that they have a coherence on some scale Λ in order that they produce interferences. This scale defines a small volume where the electromagnetic beam gives rise to interferences. For classical X-ray scattering experiments, the diffraction of large beams with many coherence volumes is observed. In each coherence volume $\mathcal{D}_i$, a wave $A_i(\mathbf{q})$ is diffracted. Only an incoherent sum of the intensities over a large number of domains N is measured:

$$I(\mathbf{q}) = \sum_{i \in N} |A_i(\mathbf{q})|^2. \tag{1}$$

With the new synchrotron sources, the high brilliance and the small source size open the possibility of obtaining coherent X-ray beams of reasonable intensity and of nearly macroscopic spatial extension. As the X-ray source is not coherent, the method consists in selecting, in the two transverse directions, a part of the incoherent beam which fulfils the conditions for diffraction:

$$\sigma\sigma' \simeq \lambda/4\pi, \tag{2}$$

where σ' is the r.m.s. divergence of the beam and σ is the r.m.s. beam size. The equality in equation (2) corresponds to fully coherent Gaussian beams. Equation (2) is in fact another version of the Heisenberg equation, if one estimates $\Delta p = 2\pi\hbar\sigma'/\lambda$ and $\Delta x = \sigma$. In practice, owing to optics, especially with the use of slits in the sample vicinity, the beam cannot be considered as Gaussian, and the condition for obtaining an X-ray beam of good coherence can be written as

$$\phi\epsilon \leq \lambda, \tag{3}$$

where ϕ is the size of the beam (usually slit aperture or pinhole diameter) and ϵ is the FWHM divergence of the beam. This rough formula always gives excellent estimates of the coherence conditions. Formula (3) has a simple physical interpretation: coherence is the high-resolution limit of a diffraction experiment, which means that the resolution $\delta q = 2\epsilon\pi/\lambda$ cannot be smaller than $2\pi/\phi$. For a very high resolution in q space, it is necessary to increase the size of the coherently irradiated sample, as for instance in Petukhov *et al.* (2006) where this size had to be extended to 100 µm for carrying out measurements with a microradian angle resolution.

Along the longitudinal direction, the diffracted waves can interfere if the FWHM path-length distribution of the waves in the irradiated sample $\Delta\mathcal{L}$ fulfils

$$\Delta\mathcal{L} \leq \Lambda_l = \lambda^2/2\delta\lambda, \tag{4}$$

where Λ_l is the longitudinal (temporal) coherence length. The optics determines the experiment monochromaticity $\delta\lambda$. One can also imagine that monochromaticity is achieved by an energy-sensitive detector.

Coherent scattering methods were first developed for the study of fluctuations in dynamical processes by means of speckle dynamics. This was a transposition of the methods of dynamical light scattering (DLS) and it is often called X-ray photon correlation spectroscopy (XPCS) or X-ray intensity fluctuation spectroscopy (XIFS). The main advantages of X-rays are in their ability to observe order fluctuations in the vicinity of Bragg peaks, to observe fluctuations at smaller sizes

(larger |**q**| values), and also in their penetration depth, which opens the possibility of studying opaque or strongly multiply diffracting samples. Fluctuations of a stationary process can be studied from the intensity–intensity correlations averaged over a large number of fluctuation times:

$$\gamma(\mathbf{q}, t) = \langle I(\mathbf{q}, t')I(\mathbf{q}, t + t')\rangle_{t'} / \langle I(\mathbf{q}, t')\rangle_{t'}^2, \qquad (5)$$

where the time covariance has been normalized by the average intensity squared. This average, obtained at a given **q**, assumes that the system is ergodic. The position of the XPCS technique in the time *versus* q domain is compared with other techniques in Fig. 1.

In coherent experiments, the first problems were to improve the experimental stability and to find suitable detectors. For XPCS, the conditions of equations (3) and (4) could be somewhat relaxed because the observation of speckles does not need a very high degree of coherence. Progress in experimental set-ups and in micromechanics quickly opened the possibility of using coherent scattering in the study of small objects where ϕ in formula (3) is the sample size. In this case, one observes the modulus of the amplitude of the wave scattered by the sample, corresponding to the Fourier transform (FT) of the electron density of the sample, and one is able to obtain direct-space information on the shape and the inner structure of the diffracting object. This leads to the recent fast development of lensless imaging methods, where phase reconstruction is achieved from measurements over-sampling the reciprocal space (Fienup, 1982, 1987). A discussion of the limits of this method can be found in Shen *et al.*

(2004) as regards intensity limitations and in Mielenz (1999) as regards resolution limitations.

Coherent X-rays is now a well established technique, and valuable information complementary to this paper can be found in van der Veen & Pfeiffer (2004) and in Lengeler (2001). Many of the methods developed for light scattering experiments are now used with X-rays. One of them is to obtain interferences between a reference and the sample, which is called heterodyning. Homodyne and heterodyne XPCS measurements provide correlation functions (Berne & Pecora, 2000) different from equation (5) and heterodyning the amplitude diffracted by the sample with that of a reference can provide a method for phase retrieval (Gabor *et al.*, 1971).

In this paper, I will show how coherent X-ray scattering experiments are carried out and discuss the progress in this field. I will limit the discussion to X-rays of energies $E > 700$ eV, *i.e.* the L edges of $3d$ transition metals.

Coherence is obtained either by selecting a part of the incoherent beam with slits or by the small size of the diffracting sample. These experiments have special needs in beamline set-ups, and the experimental problems in developing this technique will first be explained. Typical results in the XPCS technique and in lensless imaging will be summarized. Finally, the future of coherent X-ray scattering and some new developments will be discussed.

2. Coherent beam

2.1. The synchrotron sources

The intensity I_c available from a source in a coherent scattering experiment is connected to the average source brilliance $\mathcal{B}$:

$$I_c = \mathcal{B}(\lambda/2)^2(\delta\lambda/\lambda). \qquad (6)$$

The source can have a wide energy spectrum (bending magnets, wigglers) or can be narrowly peaked (undulators).

Fig. 2 shows the typical brilliance evolution among various X-ray sources. Fig. 3 shows the standard wavelength depen-
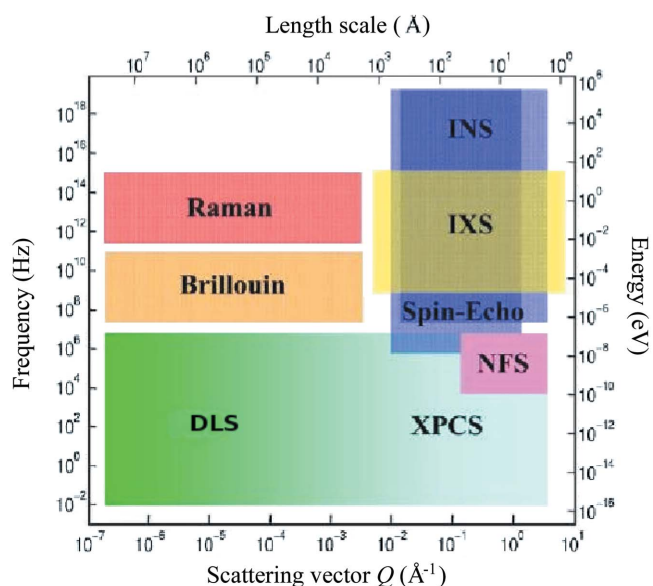
Figure 1
The frequency–scattering vector domains of available techniques for dynamic studies [adapted from Grübel & Zontone (2004)]. The XPCS domain can be extended down to $q \simeq 3 \times 10^{-4}$ Å^{-1} and $\nu \simeq 10^{-4}$ Hz, overlapping with DLS. The other techniques are inelastic neutron scattering (INS), inelastic X-ray scattering (IXS) and nuclear forward scattering (NFS).
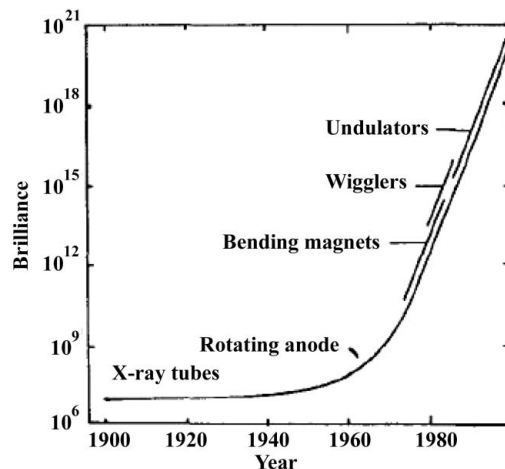
Figure 2
Summary of the source brilliance evolution during the 20th century. $\mathcal{B}$ units are photons (s mm^2 mrad^2 0.1% bandwidth)$^{-1}$.

dence of $\mathcal{B}$ for realistic undulators or bending magnets in a typical third-generation source. These estimates are for Soleil, France, but they are of the same order in many recent 'national' synchrotron sources (SLS in Switzerland, Diamond in UK, Elettra in Italy), which are in the 2–3 GeV range. A recent review of existing and future synchrotron sources is found in Bilderback *et al.* (2005), and it is interesting to refer to Helliwell (1998) for history. Sources in the 6–8 GeV range, like ESRF, APS and SPring 8, have the main advantage of providing larger brilliance in the higher-energy range ($E > 8$ keV). Units of $\mathcal{B}$ are photons s^{-1} mm^{-2} mrad^{-2} for a 0.1% bandwidth, and undulators typically provide $\mathcal{B} \simeq 10^{20}$ in the 8 keV range. In this paper, orders of magnitude will be given for the ESRF, well experienced by the author, but all third-generation synchrotron sources should be of the same order of magnitude. A 25 m long undulator (780 periods of 32 mm) at SPring-8 (Yabashia *et al.*, 2001; Hara *et al.*, 2002) could have the highest available value: $\mathcal{B} > 10^{21}$. As an example, a 'U20' undulator with an Si$_{(111)}$ monochromator ($\delta\lambda/\lambda = 1.4 \times 10^{-4}$) can provide a coherent intensity of $I_c \simeq 0.6 \times 10^{11}$ photons s^{-1} at 8 keV, from the $\mathcal{B}$ values of Fig. 3.

2.2. The beamline optics

This large intensity is somewhat reduced by the insertion of optical elements in the beam path and by the difficulty in obtaining the high degree of precision needed for light beams of subnanometric wavelengths.

A first example was diffraction from beryllium windows observed at the initial stage of the ESRF (Cloetens *et al.*, 1996). The diffraction from windows was then systematically studied (Suzuki *et al.*, 1998) and in the beamline design the choice of beryllium polished windows, crystalline diamond windows or in-vacuum beam is now one of the first subjects of discussion. The scattering from unpolished windows is not only an imaging problem, as for instance in Cloetens *et al.* (1996), where the diffraction from crystal defects was hidden

Figure 3
Estimates of brilliance of various sources for the Soleil synchrotron (France). Brilliance ($\mathcal{B}$) units are photons (s mm^2 mrad^2 0.1% bandwidth)$^{-1}$.

by the plane-wave distortion (Suzuki *et al.*, 1998). In fact, the windows also behave as secondary sources (Pietsch *et al.*, 2005), which has the effect of reducing the source brilliance. For instance, in Pietsch *et al.* (2005), the beam coherence was discussed by considering that the source was at a distance of 7.6 m (the unpolished beryllium window acting as a virtual source) and not at the electron beam position 45 m away. This is a strong effective brilliance reduction of the source.

2.2.1. Focusing. In a synchrotron experiment, the source-to-sample distance is of the order of 50 m, and the FWHM source height is between 20 µm (an undulator beamline at ESRF) and 70 µm (a bending magnet beamline of ESRF). From equation (3), one calculates the vertical transverse coherence length at the sample: $\Lambda_v \simeq 400$ µm. The horizontal FWHM of the beam is close to 1 mm (in the case of even undulators of the ESRF like ID10), and $\Lambda_h \simeq 8$ µm. This is one of the reasons for having beams in the $\phi \simeq 10$ µm range for speckle experiments. In this case, only a small part of the available intensity is selected in the vertical direction. Vertical focusing can compensate for this problem: the intensity is increased in the same proportion as Λ_v is decreased. The ratio between the source-to-focusing-optics distance and the optics-to-sample distance has to be of the same amount as the ratio between the source height and the pinhole diameter, *i.e.* about two in this case. For the study of nanoobjects, where the beam coherence length can be reduced, this ratio can be much larger, and the focusing set-up can be very close to the sample, opening the possibility of submicrometre focused beams.

Coherent experiments need high-quality focusing elements. To this end, different techniques have been developed.

(*a*) Refractive lenses use the slightly smaller than unity index of refraction of matter (Snigirev *et al.*, 1996; Lengeler *et al.*, 1999). They currently provide focused beams of 3 to 10 µm with a metre range of focal lengths (Lengeler *et al.*, 1998) in beamlines like ID01 of ESRF and a typical focus size of 30 µm FWHM for a focal length of about 15 m at ID10. These (relatively) large focus sizes could be explained by lens imperfections, but also by large focal distances. This typical size of the focused beam at the sample was well adapted for speckle experiments, where the beam was in the 10 µm range. For imaging purposes of submicrometre samples, shorter focal distances (less than 1 m) and submicrometric beams are now currently available, thanks to novel mechanical techniques (Lengeler *et al.*, 2002). A discussion of the recent improvements in focus size and in energy range is given in Schroer *et al.* (2003) and Lengeler *et al.* (2005). Absorption limits the use of lenses to X-ray energies larger than 5 keV.

(*b*) Phase zone plates (Fresnel zone plates, FZP) can give very small focus sizes and they also benefit from the advances in microprocessing. Their initial efficiency of the order of 10% (Yun *et al.*, 1999) could be raised by a suitable choice of material (David *et al.*, 2001). Complex multilevel zone plates can reach 50% efficiency (Fabrizio *et al.*, 1999) and even more (Nöhammer *et al.*, 2003).

These two focusing methods are now well developed [see David *et al.* (2004) for some descriptions of the set-ups]. They have chromatic aberrations: their focal distances have a strong
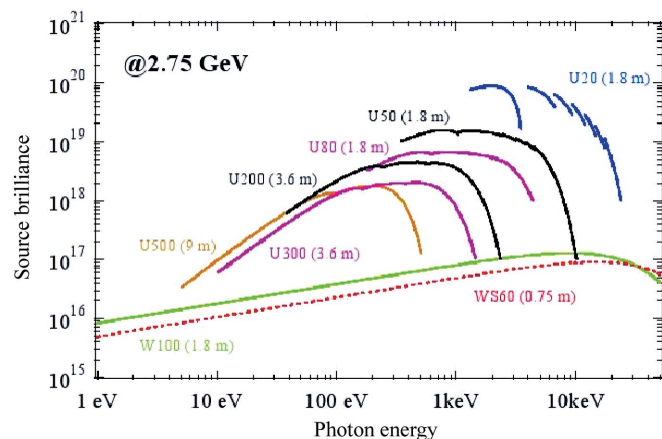
λ dependence (λ^{-2} for refractive lenses and λ^{-1} for FZP). Their shape and the choice of the material have to be adapted to the chosen energy range and focal distance. Their focusing characteristics now reach the diffraction limits.

(c) Mirror design is an important parameter of the beamline optics. These are used as low-pass filters and as focusing elements. In the first ESRF design, the vertical emittance was planned to be 0.7 nm rad, with a 10% coupling between horizontal (7 nm rad) and vertical emittance. The ESRF emittance is now about 4 nm rad horizontally and the coupling has been reduced to less than 1%. The vertical source size was therefore reduced by a factor of 25 compared to the first design. The standard vertical source sizes of undulators in large facilities (ESRF, APS and SPring 8) are close to the ESRF value: 8 μm (r.m.s.). The first mirrors were long (1 m at least) and their r.m.s. slope errors were of the order of 5 μrad. For a source-to-focusing-mirror distance of 30 m and a mirror-to-sample distance of 15 m, the FWHM height of the beam should be 10 μm with a perfect mirror. With the initial mirror specifications, the slope errors induce a 350 μm FWHM height. This yields a loss of a factor of 35 in the source brilliance. In a non-coherent experiment, the image of the focused beam when studied in detail then consists of a superposition of spots corresponding to various parts of the mirror. Each spot can have the size of the focused source (about 10 μm). This can induce large experimental instabilities for small samples or in high-resolution diffraction experiments. In the present description, from equation (3), the vertical transverse coherence length at the mirror is $\Lambda_v \simeq 220$ μm, for a 30 m distance from an undulator source. In this case, only a few centimetres of the mirror are selected and slope errors are less of a problem, because one chooses a 'good region' of the mirror, i.e. a strong maximum in the beam profile. Some improvements have been made in the polishing of large mirrors and slope errors for large mirrors are now of the order of 1 μrad (r.m.s.). Further progress is obtained from active bending and by the reduction of the size of the mirrors. For coherent systems (Hignette et al., 2001), the relevant quantity is the mirror shape error Σ and Marechal's criterion states that

$$\Sigma \simeq \lambda/[27 \sin(\theta_c)] \simeq 1\,\text{nm} \qquad (7)$$

for classical critical angles θ_c. These characteristics are now obtained by combining interferometric measurements with chemical machining and plasma etching of the surface (Yamauchi et al., 2002; Yamamura et al., 2003). These mirrors are used in the Kirk–Patrick–Baez (KB) configuration for focusing at short distances with a very small focus (<1 μm). Mirrors are very efficient because of their small intensity losses and their nearly energy independent focusing properties. Another method for reducing the size of the mirror was to increase the incidence angle by replacing the mirror by a multilayer. In Ziegler et al. (2001), the multilayer had less than 1 μrad slope errors and, in Hignette et al. (2005), sub-100 nm focusing was obtained.

These focusing methods are now well developed and very small beam sizes are obtained. This opens the possibility of observing samples at a very small scale, as is currently done in scanning electron microscopy, or to have high-quality optical lenses for imaging purposes in X-ray microscopy techniques. The aim of this paper is the use of coherent X-ray beams. The sample scale studied is usually larger than 1 μm for speckle experiments. For the lensless imaging technique, the beam can be significantly larger than the sample, and the main problem is to ensure that the sample is irradiated by a plane wave in order to use the fast Fourier transform (FFT) algorithms. This problem has been briefly discussed (Robinson et al., 2003) in the case of a non-planar focused beam and Kohmura et al. (2005) has examined the effect of wave distortion occurring after a pinhole. This, combined with the irradiation problems arising from excess intensity, nowadays probably limits the need of very small beam sizes in the experiments discussed here.

2.2.2. Monochromatization. Another aim of optics is wavelength selection. This selection is an important experimental parameter for the longitudinal (temporal) coherence. XPCS experiments are often performed in the vicinity of 8 keV, except for resonant scattering experiments, but higher-energy X-rays may be a valuable choice (Thurn-Albrecht et al., 2003).

Energy selection can be performed using three techniques: filters ('pink beam'), crystals, and grates or multilayers.

(i) Pink beam selects a harmonic of an undulator with mirrors and absorbing filters [Abernathy et al. (1998) (at ESRF) and Sandy et al. (1999) (at APS)], and the resulting bandwidth is $\delta\lambda/\lambda \simeq 1.3\%$ (r.m.s.) for both synchrotrons. Fig. 4 shows the energy distribution of a typical undulator of the APS and the result of low-pass filtering by a mirror. With the quality and the length of modern undulators, this value of $\delta\lambda/\lambda$ is essentially dependent on the characteristics of the electronic optics of the synchrotron (essentially the horizontal emittance of the synchrotron and secondarily the horizontal 'beta function' of the beamline).
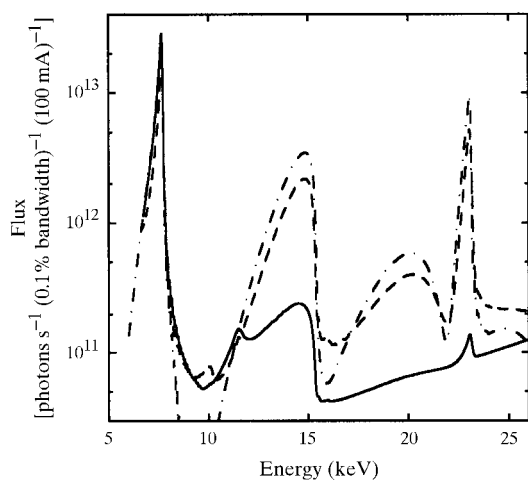
Figure 4
The energy dependence of the flux of an APS undulator, as calculated (dot-dashed line), as measured after a Pt-coated mirror which reflects all wavelengths (dashed line) and after a silicon mirror acting as a low-pass filter ('pink beam', continuous line). (Adapted from Sandy et al., 1999.)

(ii) Crystals are used in most cases. As distortions of the crystallographic planes in imperfect crystals have the same effect as mirror-slope errors, perfect crystals are used, which limits the bandwidth possibilities. The larger energy bandwidth is $\delta\lambda/\lambda \simeq 3 \times 10^{-4}$ with the $Ge_{(111)}$ Bragg reflection (Hart & Berman, 1998). This bandwidth is reduced to $\simeq 10^{-8}$ in inelastic scattering beamlines (Verbeni *et al.*, 1996; Toellner *et al.*, 2001), which means that the longitudinal coherence lengths vary from the µm to the cm range.

(iii) Monochromatizing reduces intensity. Some experiments need intermediate energy resolution. Multilayers (Morawe *et al.*, 2003; Martynov *et al.*, 2004; Hignette *et al.*, 2005) can become very useful, and the number and the quality of the layers has been improved (Liu *et al.*, 2004). Light-element multilayers of high quality and of a large number of periods are now available (Platonov *et al.*, 2004). These provide excellent monochromators for small-angle scattering experiments (SAXS) and for the study of nanocrystals, where the longitudinal coherence length Λ_l can be small. For low X-ray energies, where Bragg scattering cannot be used, gratings provide adjustable monochromaters. The efficiency of gratings for soft X-ray optics was discussed in Attwood *et al.* (1999). One characteristic feature was the low overall efficiency of this type of set-up at the X-ray energies discussed here: there was a 10% efficiency of the gratings and another order of magnitude was lost in optics aberrations. New improved optics are now developed around the synchrotrons more dedicated to this energy range (ALS, Elettra).

2.3. X-ray detection

2.3.1. Detection. Coherent diffraction is the high-resolution limit of incoherent diffraction. As both incident $\mathbf{k}_i$ and diffracted $\mathbf{k}_f$ wavevectors determine the resolution volume, equation (3) is also valid for detection. In an XPCS experiment, the sample-to-detector distance is of the order of 2 m and the aperture of the detector is of the order of 20 µm. This gives $\epsilon_d \simeq 10$ µrad and, from (3), ϕ must be in the 10 µm range for a 1.6 Å wavelength. This is the main reason for choosing this beam diameter in XPCS. If the sample size is the beam aperture, like in nanocrystal studies [see for instance Robinson *et al.* (2001), where crystals are in fact in the micrometre range], ϕ is significantly smaller and ϵ_d can be increased.

2.3.2. Point detectors. With slits and a point detector, the resolution can be easily adjusted. Combining these detectors with fast correlators is a very efficient method for the study of fast phenomena, but large intensities are necessary. One can estimate the statistical error in γ in equation (5) for low counting rate (Fera *et al.*, 2000):

$$\Delta\gamma(\mathbf{q}, t) \simeq [\gamma(\mathbf{q}, t)]^{1/2}/[I(\mathbf{q})(T\Delta t)^{1/2}], \qquad (8)$$

where $I(\mathbf{q})$ is the measured intensity per unit time, T is the total measuring time and Δt is the sampling time. A detailed discussion of the errors is found in Brown (1993). With the good stability of available beamlines, T can be extended to a few thousand seconds and, from the measured intensities I, the

minimum accessible Δt can be easily estimated. As the correlator can sample a very short time interval, the time structure (bunches, ...) and all beamline and synchrotron vibrations or drifts are observed.

2.3.3. CCDs. For X-ray imaging of the scattered intensities in reciprocal space and for slow processes with low counting statistics, area detectors are currently used.

For the high resolution necessary in these measurements, direct illumination CCDs (DI-CCD), provide a reasonable detection quantum efficiency (DQE) in the 0.1–12 keV energy range. In Fig. 5 is plotted the DQE energy dependence of the two main CCDs used in such experiments. The left curve corresponds to the front-illuminated 'deep-depletion' CCD (DD-CCD) and the right curve to the 'back-illuminated' (BI-CCD) one.

In DD-CCDs, the X-rays are detected close to the integrated circuit surface, in the vicinity of the CCD cell, and the charges are spread over a distance smaller than the pixel size, which is of the order of 20 µm. These CCDs are made from high resistivity ('deep depletion') silicon wafers. In BI-CCDs, the wafer is thinned to about 50 µm and X-rays are absorbed on the opposite size and detected at the surface. As both of these CCDs directly absorb X-ray photons in the Si wafer, a large number of charges n_e are detected. For an X-ray energy E (in eV), $n_e = E/3.62$ is a classical formula. As CCD cells saturate at about 200000 electrons, *i.e.* 100 photons pixel^{-1} at 8 keV, it is necessary to read the CCD frequently in order to avoid saturation. On imaging, a large number of frames have to be added.
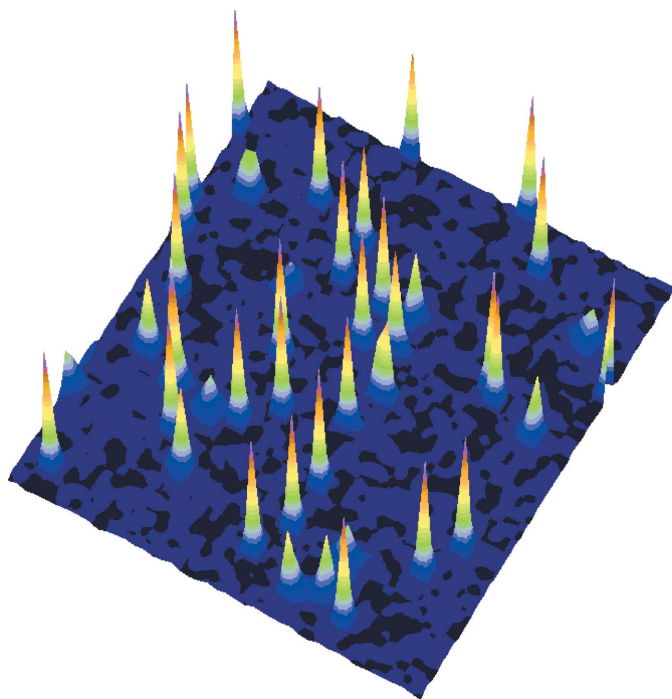
For dynamical studies, the sampling frequency of the CCD is an essential parameter which limits the minimum sampling time Δt. High-quality CCDs have a slow frequency (1 MHz), in order to limit electronic noise to less than 10 electrons. When used as 'indirect' detectors (*i.e.* with an X-ray-to-optical-light conversion), only a few electrons per X-ray are detected and a very low noise is necessary. In DD-CCDs or BI-CCDs, the signal-to-noise ratio is much larger, and increasing the frequency by a factor of ten should still induce an
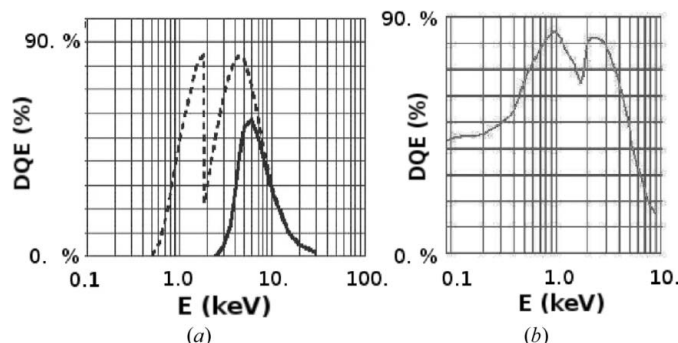
Figure 5
Dependence of the DQE on photon energy (in keV) for the CCDs used in coherent scattering experiments. (*a*) Direct illumination, with (continuous line) and without (dashed) beryllium window. (*b*) Back illumination, no window (adapted from Princeton Instruments data sheets).

acceptable noise. For instance (Falus *et al.*, 2004), with a classical CCD (lower DQE than the DD-CCD of Fig. 5), the full frames (1024 × 1024 pixels) were read at a 50 Hz repetition rate. Another method for obtaining short Δt is the kinetic mode, where only a small part of the CCD is used (Lumma, Lurio, Mochrie & Sutton, 2000). As multiple exposures of the same frames are used, the time between two samples can be reduced to the shift time, of the order of one hundredth of a microsecond.

In both dynamical and imaging uses of CCDs, a number of frames have to be managed. For small enough intensities, the CCD can be used as a 'photon counting detector' (Livet *et al.*, 2000). Fig. 6 shows a small part of a DD-CCD where individual X-rays can be observed. In this DD-CCD, the charges produced by the absorption of an X-ray photon are mainly localized on one or two pixels and it is not difficult to locate the impact. This method gives a very efficient noise suppression. One can also use the X-ray energy dependence of the charges to obtain filtered images. For very low count rate, this opens the possibility of removing fluorescent scattering, cosmic rays or harmonic components from the beam. Obtaining 'true' countings also gives a very good estimate of errors by means of Poisson statistics. This method has been extended to soft X-ray imaging (Chesnel *et al.*, 2002) and now to BI-CCDs. For BI-CCDs, electronic charges induced by the absorption of 700 eV X-rays are spread over a distance corresponding to 2–3 pixels (with 14 µm BI-CCD pixel sizes).

The center of mass of the electronic cloud from each X-ray is obtained with a precision of less than 1 pixel, yielding a better resolution than simply adding frames. This 'droplet' algorithm was combined with the kinetic mode (Livet *et al.*, 2006).

The DD-CCDs are efficient in coherent scattering experiments for $\lambda < 2$ Å when the intensity is low, but as X-rays are front-absorbed, some radiation damage is observed. For lower X-ray energies, the BI-CCDs have a better DQE and no significant radiation damage occurs because the X-rays are absorbed on the opposite side of the CCD. As the charges have to migrate across the CCD, they are spread over a few pixels.

For large intensities, new 'pixel array detectors' are under development, where each pixel can count 10^7 X-rays s^{-1} (Rossi *et al.*, 1999; Delpierre *et al.*, 2001). Pixel sizes were of the order of hundreds of µm (Bérar *et al.*, 2002; Löcker *et al.*, 2004; Broennimann *et al.*, 2006) but rapid improvements are happening with 170 µm resolution (Pfeiffer *et al.*, 2003) and now 55 µm (Pfeiffer *et al.*, 2004; Zorzia *et al.*, 2005; Bisogni *et al.*, 2006). These area detectors with a 50 µm resolution will probably become standard for high-intensity XPCS measurements.
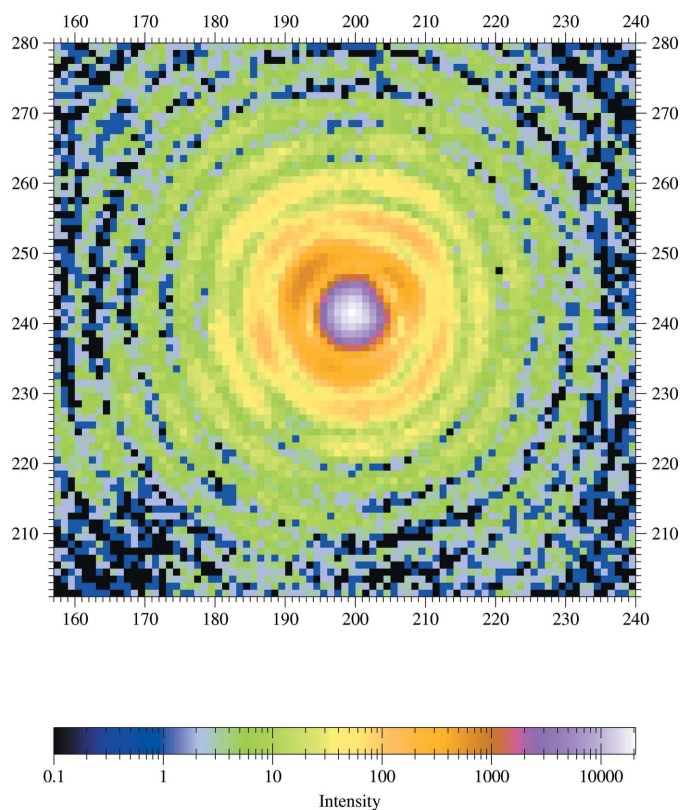

Figure 6
Observation of individual X-rays in a small part of a DD-CCD. The charges are essentially on one pixel, a few on two. The total number of charges of each peak is connected to the X-ray energy: here $E = 8$ keV (unpublished results).

Figure 7
Diffraction from a circular pinhole of diameter $\phi = 5$ µm, $\lambda = 3.3$ Å, detector with 22 µm pixels at 1.8 m. This image results from the accumulation of 2000 DI-CCD frames. For each frame, the CCD was transformed in a photon-counting detector, as described in Livet *et al.* (2000). Intensities correspond to counts, and the log units show the large dynamics obtained (unpublished results obtained at the ID20 beamline of ESRF).

3. Observation of speckles

3.1. Pinholes and slits

In first coherent scattering experiments, laser-drilled holes in 50–100 µm thick Pt sheets were used (Sutton *et al.*, 1991).

For speckle dynamics experiments, the exact shape of the pinhole is not very relevant, and the input wavefront need not be planar. For carrying out coherent experiments, one first check was provided by the observation of the Frauenhofer fringes from pinholes. The shape of the scattering was somewhat irregular. The reason could be the poor quality of the beamline optics, giving multiple beams crossing the pinhole as well as the pinhole's irregular edges. When electrochemically drilled pinholes developed for electron microscopy became available, beautiful pinhole diffraction could be obtained (Livet *et al.*, 1998), as shown in Fig. 7. Now with ion-beam machining, well controlled hole shapes can be obtained and one can measure various interference patterns (Leitenberger *et al.*, 2003; Eisebitt, Lörgen *et al.*, 2004). For XPCS measurements, it is useful to continuously change the beam aperture in a reproducible way. The recent progress in micromechanics enables routine submicrometric positioning of slits. Some studies were necessary for a better understanding of slit-edge scattering. This problem was addressed in

Nikulin & Davis (1988) and the refraction of wedge-shaped edges was measured. Edges behave like a prism, with a strong scattering at very small angles, depending on the refractive index of the slit and on the wedge angle. In Vlieg *et al.* (1997), the wedge angle was reduced to 0.5° and refraction was almost suppressed. As available motors now make slit positioning reproducible with an accuracy of a few hundred nanometres, careful studies of slit scattering were performed.

Fig. 8 shows the diffraction of 1 µm square slits, with a 1 mm distance between carefully polished roller blades along the beam path. This distance explains the asymmetry of the pattern. A quantitative study (Le Bolloc'h *et al.*, 2002) of the scattering of these slits showed that the observed intensity could be explained by the intrinsic Frauenhofer scattering of the slits. This wave calculation was used in order to discuss the efficiency of guard slits for background reduction in coherent SAXS (CSAXS) (Livet *et al.*, 2003). Measured and calculated scattering from 1 µm asymmetric slits showed very good agreement. The calculation of a plane wave propagating through a 'macroscopic' object (here the 1 µm asymmetrical square slits) shows that our diffraction figure does correspond to the real object and that our experiments are reliable enough to reconstruct the shape of diffracting samples.

Now nearly ideal diffraction patterns can be obtained from all apertures and slits are often preferred because of their flexibility in XPCS. An aperture modifies the shape of the
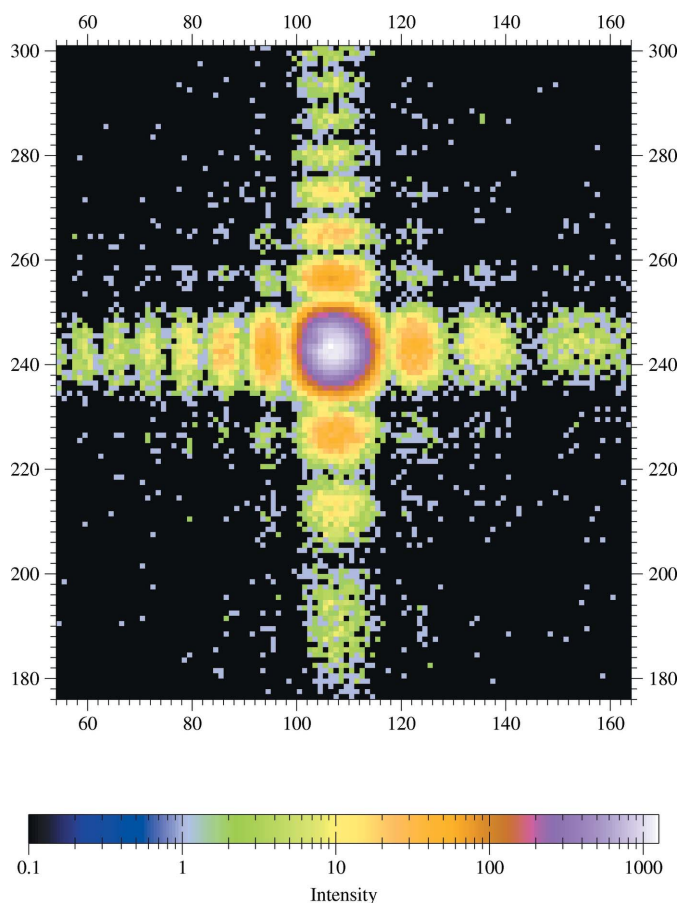
Figure 8
Diffraction from 1 µm asymmetric square slits, $\lambda = 1.58$ Å, detector with 22 µm pixels at 1.25 m. Slit edges are 1 mm distant along the beam path (unpublished results from the BM2 beamline of ESRF).
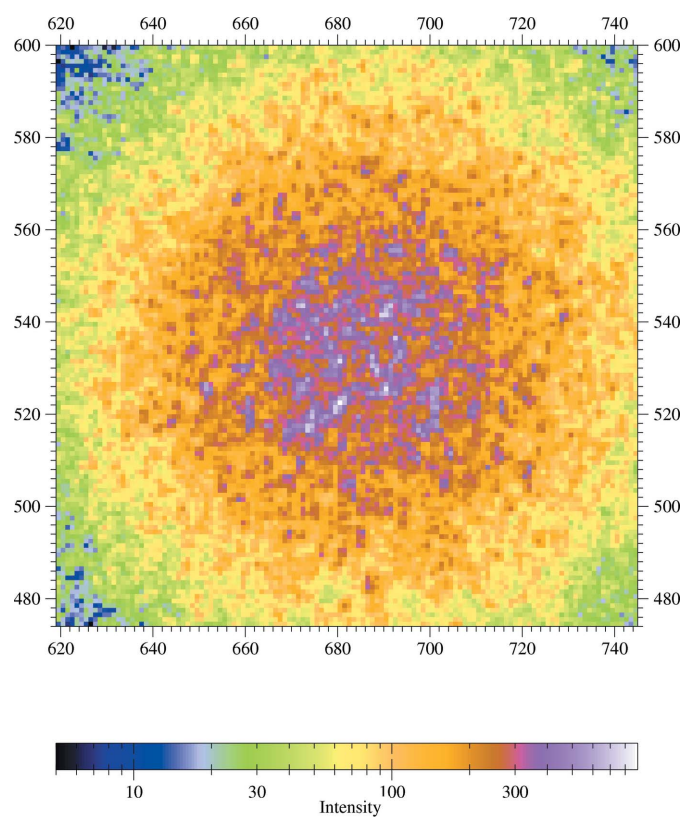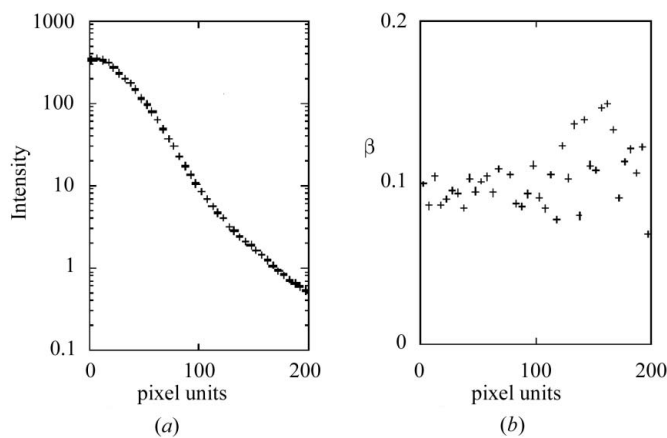

Figure 9
Diffraction from an ordered $AuAgZn_2$ alloy at the $(\frac{1}{2}\frac{1}{2}\frac{1}{2})$ Bragg superstructure position. $\lambda = 1.58$ Å, 12 µm² slits, detector with 22 µm pixels at 2 m (unpublished results from the ID10 beamline of ESRF).

propagating plane waves, and one can distinguish the near-field (NF) region from the far field (FF) region. For distances much larger than the NF/FF limit $\mathcal{F} = \phi^2/(2\lambda)$, the FF image of the pinhole exhibits a large diffraction pattern, as shown in Figs. 7 and 8. For this reason, in SAXS, adding guard slits is necessary. In CSAXS, all parasitic background from the sample vicinity can interfere with the sample scattering, making subtraction of a background intensity impossible. This is connected to the large longitudinal range e where a wave can interfere for a given scattering angle θ in SAXS:

$$e \simeq \Lambda_l/(2\theta_m^2). \tag{9}$$

In CSAXS, the minimum θ value θ_m is of the order of, or less than, 10^{-3} rad [$q_m = 4\pi \sin(\theta_m)/\lambda \simeq 8 \times 10^{-3}$ Å^{-1}] and $e \simeq 0.25$ m with an Si$_{(111)}$ monochromator. Even if this parasitic intensity is many orders of magnitude lower than the beam, for low scattered intensity, it may still dominate significantly the signal from the sample. Low parasitic scattering is also very sensitive to small defects of the aperture edges, making the amplitude scattered by the slits difficult to estimate. Moreover, these interfering amplitudes can give rise to some heterodyning in dynamic CSAXS experiments (Livet et al., 2006). The guard slits are positioned close to the sample, at a distance of the order of $\mathcal{F}$. This set-up produces a strong cross-shaped background and cross beamstops yielded SAXS measurements with very low background (Livet et al., 2003). Another method uses asymmetric slits and limits measurements to the region of the diffusion plane where slit scattering is minimum (Abernathy et al., 1998; Sandy et al., 1999; Lumma, Lurio, Borthwick et al., 2000). In large-angle measurements (WAXS), beam background reduction is not a problem and guard slits are useless. In an imaging experiment, like in diffraction from nanoparticles (Robinson et al., 2001), the exact shape of the wavefront is an important parameter and closing slits before the sample significantly modifies the diffracted intensity (Kohmura et al., 2005).

Figure 10
Angular average (log scales) (a) of the intensities of Fig. 9 over a 5 pixels ring and the corresponding estimated coherence β (b). Pixel units are distances to the central peak in Fig. 9, i.e. 4.4×10^{-5} Å^{-1} per pixel.

3.2. Estimating coherence

The coherence properties of a monochromatic radiation at the sample position are defined by the complex unnormalized mutual coherence function of the electromagnetic wave:

$$\Gamma(\mathbf{r}_1, \mathbf{r}_2) = \langle E(\mathbf{r}_1, t)E(\mathbf{r}_2, t)^* \rangle_t. \tag{10}$$

This function can be studied by 'Young's double hole' experiments where the interferences are measured between the two points in the beam $\mathbf{r}_1$ and $\mathbf{r}_2$. The visibility of the fringes (Born & Wolf, 1980) $\mathcal{V}$ is connected to Γ, normalized by $[I(\mathbf{r}_1)I(\mathbf{r}_2)]^{1/2}$, where $I(\mathbf{r}) = \Gamma(\mathbf{r}, \mathbf{r})$ is the intensity at $\mathbf{r}$. This type of experiment is now currently made possible with the progress in nanotechnologies (Paterson et al., 2001; Leitenberger et al., 2003; Tran et al., 2005; Pietsch et al., 2005) because high-quality holes of micrometre sizes are necessary. An interferometric method was used in order to obtain a direct measurement of $\mathcal{V}(\mathbf{r}_1, \mathbf{r}_2)$ (Pfeiffer et al., 2005). The Fresnel mirrors technique (Marchesini et al., 2000) also gave excellent results. An elementary method for checking coherence is also to observe pinhole Frauenhofer diffraction (Sutton et al., 1991; Panzner et al., 2003). In this case, the amplitude of the oscillations provides a rough estimate of the visibility $\mathcal{V}$.[1]

In speckle experiments, the interference of the whole irradiated sample is studied, and one needs estimates of the average value of $|\Gamma|^2$ across the irradiated sample. For X-rays, a comparison between calculated and measured coherence is important for improving the reliability and the reproducibility of this type of experiment. In static scattering, speckles appear as rapid modulations of the intensity when the incoherent intensity should be only slowly varying. Fig. 9 shows the speckle structure of the $(\frac{1}{2}\frac{1}{2}\frac{1}{2})$ superstructure of the Heussler ordered AuAgZn$_2$ alloy. Owing to quenching, the Bragg peak is broadened by the finite size of the ordering domains (Livet et al., 2002). In an incoherent experiment, the peak is isotropically broadened and, in a coherent experiment, it acquires a speckle structure. The intensity statistics of fully coherent scattering follows an exponential law. A simplified theory of partial coherence assumes that the intensity in equation (1) is the result of adding N contributions all having the same probability distribution from various volumes of coherence, and that all these volumes have the same probability distribution. In this case, the speckle intensities should be distributed according to an Nth-order Γ_N distribution. The second moment of the intensity distribution can be calculated from the static intensity variations and the coherence degree β is defined from

$$1 + \beta(q) = [\langle I(\mathbf{q})^2 \rangle - \langle I(\mathbf{q}) \rangle]/\langle I(\mathbf{q}) \rangle^2. \tag{11}$$

In this equation, the averages $\langle \rangle$ are carried out in a $\mathbf{q}$ domain where the incoherent intensity can be assumed constant. A Poisson contribution $\langle I(\mathbf{q}) \rangle$ has to be subtracted from the experimental value of the mean square deviation.

---

[1] One has to be careful with this type of estimate: the contrast observed in the asymptotic oscillations of the pinhole diffraction is essentially connected to the mutual coherence of the electromagnetic wave at the edges of the aperture.

This method can be applied to Fig. 9, where the 'droplet algorithm' had transformed for each frame the CCD into a photon counting detector (Livet *et al.*, 2000), and where 100 frames have been added. Fig. 10 shows the intensity averaged over five-pixels-width circular rings around the center of the Bragg peak and the estimates of $\beta(q)$. In this case, $\beta \simeq 0.1$, independent of q, for three orders-of-magnitude variations of the intensity. Reliable estimates could be obtained even from regions of low intensities (less than 1 photon pixel^{-1}) because of averaging over a large number of pixels.

Another method is to study the speckle autocorrelation from the covariance between neighboring pixels. In the case of figures similar to Fig. 9, this function has a slow variation due to the convolution product of the incoherent intensity and a fast peaked one due to the speckle structure. If Poisson counting statistics can be neglected, the ratio between the maximum of the peak and the 'plateau' is a good estimate of $1 + \beta$ (Tsui *et al.*, 1998). With an area detector, the shape of the peak obtained by this method is directly connected to the experimental geometry of the coherence volume, as it is observed in the conditions of 'pink beam' (Abernathy *et al.*, 1998; Tsui *et al.*, 1998; Sandy *et al.*, 1999), where speckles were elongated by the poor energy resolution, or in asymmetric Bragg scattering (Pitney *et al.*, 2000).

The static contrast is connected to the number of areas of coherence: $\beta = 1/N$ and β varies from 1 (full coherence) to 0 (no coherence). Careful studies showed that the intensity distribution was more complex than the simple model leading to a Γ_N distribution of the intensities. In Abernathy *et al.* (1998) and in Livet *et al.* (1998), it was necessary to add a small fully incoherent beam component to explain the observed distribution. This can be interpreted in the following way: the beam from which a partially coherent part is selected is not homogeneous. The beam is selected in a region of maximum intensity, but a part of this beam corresponds to a large number of coherence areas of lower intensities. These small components are essentially connected to optics imperfections, which gives fully incoherent scattering. This interpretation was also given for the observation of regions of the beam with a low visibility in Pfeiffer *et al.* (2005). These components are strongly reduced if, before selecting the beam with the pinhole of size ϕ, a first pinhole is set after the optics, at a distance D from the sample pinhole, with an aperture ϕ_1, in order to have a reproducible angle $\epsilon = \phi_1/D$ in formula (3).

3.3. Optimizing

In equation (11), $1 + \beta(q)$ is the limit for $t = 0$ of the function $\gamma(\mathbf{q}, t)$ [equation (5)], provided that the dynamic process studied fulfils the ergodic principle, and that the fluctuation time is large enough to be observable. This $t = 0$ limit is a classical way of obtaining β in DLS and, for this reason, β is called the 'zero time intercept'. If the measuring time is significantly larger than the fluctuation time, in the homodyne case, the relevant quantity in $\gamma(\mathbf{q}, t)$ is the time variable part $g^{(2)}(\mathbf{q}, t)$, which is calculated from the equation (Berne & Pecora, 2000)

$$\gamma(\mathbf{q}, t) = 1 + \beta(q)g^{(2)}(\mathbf{q}, t). \tag{12}$$

For ergodic systems, $g^{(2)}$ can be calculated by averaging over a set of pixels of an area detector:

$$1 + \beta(q)g^{(2)}(q, t) = \langle\langle I(\mathbf{q}, t')I(\mathbf{q}, t + t')\rangle_{t'}\rangle_{\mathbf{q}}/\langle\langle I(\mathbf{q}, t')\rangle_{t'}^2\rangle_{\mathbf{q}}, \tag{13}$$

where, like in equation (11), a second average is carried out in a region where the same dynamics can be assumed. This technique is also used in DLS for very small q measurements (Cippelletti & Weitz, 1999) and is often called 'multispeckles'. The error in calculating $g^{(2)}$ can be deduced from equation (8). The result can be summarized as

$$\Delta g^{(2)}(\mathbf{q}, t) \simeq [1 + \beta g^{(2)}(\mathbf{q}, t)]^{1/2}/[\beta(q)\langle I(\mathbf{q}, t)\rangle_t(T\Delta t P)^{1/2}], \tag{14}$$

where P is the number of pixels of the CCD involved in averaging in the case of an area detector. The inverse of $\Delta g^{(2)}$ is the signal-to-noise ratio (SNR), called the 'quality factor' of the experiment. A practical consequence of this expression is that the precision of the experiment is essentially dependent on the product βI for a point detector.

The quality of the set-up and an estimate of optimum conditions can be discussed from the simplified model of a coherence experiment described above, and schematized in Fig. 11: a secondary source of square aperture ϕ_1 after the optics, at a distance D before the sample, a square aperture ϕ at the sample and a detector at a distance d with square pixels of size δ. Assuming a transverse infinite homogeneous incoherent beam, the coherence of a monochromatic beam selected by two sets of square slits can be calculated by a series expansion in the variable z [$= z_1 = \pi\phi_1\phi/(\lambda D)$ here]:

$$\beta(z) = \left\{\sum_{n=0}^{\infty}(-1)^n 2^{2n+2}z^{2n}/[(2n+1)(2n+2)(2n+1)!]\right\}^2. \tag{15}$$

This equation holds for beam selection and for detection, which also reduces the contrast. An excellent approximation for the overall value of β is to write the experimental contrast as the product of the contrast of the beam and the detection contrast: $\beta \simeq \beta(z_1)\beta(z_2)$, with $z_2 = \pi\phi\delta/(\lambda d)$. The SNR of an
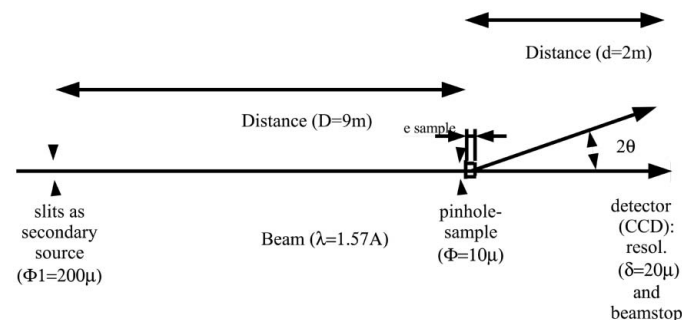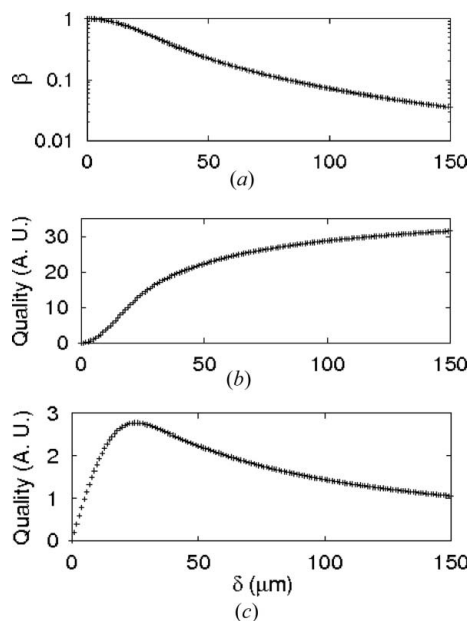

Figure 11
Schematic of a typical SAXS coherent experiment with focusing optics. Secondary source: slits of aperture ϕ_1 at $D = 9$ m from the sample, with a pinhole of aperture ϕ and a detector at $d = 2$ m, and a detection aperture of δ.

experiment can be shortly discussed from the simplified description of the experimental set-up of Fig. 11 by estimates of the following two terms.

(i) *The detector resolution.* If only the aperture δ is varied, the δ dependence of the product βI, *i.e.* the SNR of the detection of the speckles, is proportional to $z_2^2\beta(z_2)$ and this function has a constant limit for large z_2. Fig. 12 shows the results of the calculations corresponding to the set-up of Fig. 11 when δ is varying. The top curve shows the decrease of β when the point detector aperture δ is increased. The center curve shows the variation of the SNR with δ with the constant limit (units are arbitrary). We observe that reducing β from 0.3 ($\delta \simeq 20$ μm) to 0.03 ($\delta \simeq 80$ μm) causes a 60% increase in the SNR. The lower curve shows the SNR calculated by taking into account the number of pixels P when an area detector is used. The previous estimate has to be multiplied by $(P \propto 1/z_2)^{1/2}$. This curve has a maximum close to the CCD pixel size (22 μm). This shows that binning the pixels of the detector in the set-up of Fig. 11 would induce a loss in the experiment quality (*i.e.* the SNR). This discussion is also found in a recent paper (Falus *et al.*, 2006) on the Gaussian beam model, and the conclusions are similar for optimizing the detector pixel size. The important conclusion of this calculation is that the optimum for detection in a dynamic SAXS speckle experiment with a monochromatic beam and an area detector is about

$$z_2 = \pi\phi\delta/(\lambda d) \simeq 2.5. \qquad (16)$$

(ii) *The beam aperture.* In the case when a CCD is used, the pixel size δ is fixed. The variations of β and of βI versus ϕ for

various secondary source dimensions ϕ_1 are plotted in Fig. 13. These results are estimates for the set-up described in Fig. 11. One observes that, for a given secondary source size ϕ_1, βI has a maximum at a ϕ value which we define as ϕ_m. The position of ϕ_m is dependent on ϕ_1. This maximum corresponds to the compensation between the increase of the SNR with ϕ and the lowering of the detection contrast because the speckles become narrower than δ. Varying ϕ_1 from 100 μm ($\phi_m \simeq 13$ μm) to 300 μm ($\phi_m \simeq 9$ μm) increases the maximum SNR by a factor of two and decreases the corresponding β from 0.37 to 0.15.
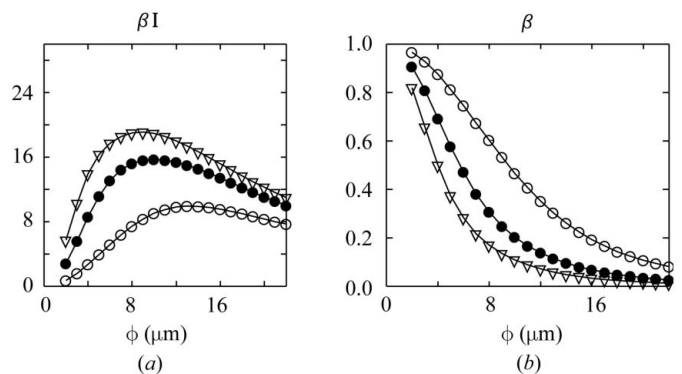
3.4. Longitudinal coherence

In a transmission CSAXS measurement, the monochromaticity of the beam fixes the length of the interfering region by equation (9), where e is the upper limit of the sample thickness and θ_m is replaced by the maximum angle θ_M. The monochromaticity in CSAXS also limits the coherence volume in the transverse direction:

$$2\phi\theta_M < \Lambda_l, \qquad (17)$$

where we have assumed that the beam size ϕ is the transverse dimension of the irradiated volume.

For a small θ_M and classical monochromators, interferences are easy to obtain for a sample thickness e of the order of millimetres and beam sizes of the order of 10 μm. For pink-beam experiments where $\Lambda_l \simeq 60$ Å, the longitudinal coherence has to be taken into account in the calculation and β becomes strongly q dependent. In Tsui *et al.* (1998) and Abernathy *et al.* (1998), this point is discussed in the Gaussian approximation. From formulae (17) and (9), one can observe that, in SAXS, wavelength distribution affects coherence by two mechanisms: for $\theta < \theta_{co} \simeq \phi/e$, the beam size is dominant [equation (17)] and, for $\theta > \theta_{co}$, it is the sample thickness (9). For a 1 mm thick sample and a 10 μm beam size, this limit is about $\theta_{co} \simeq 0.01$ rad.

For WAXS, in the vicinity of a Bragg peak, the path-length differences can be much larger. The simplest discussion is the symmetric Bragg configuration, with the formula

Figure 12
Typical dependence of the speckle contrast β versus the detector aperture δ (*a*), the variations of the SNR (or quality, in arbitrary units) for a point detector (*b*) and with δ as the CCD pixel size (*c*). Curves (*b*) and (*c*) cannot be compared. In the case of an area detector, the 22 μm pixel size, at this 2 m distance, is an optimum, and one should not bin pixels of the CCD.

Figure 13
Calculated quality factor (SNR, arbitrary units) (*a*) and the corresponding speckle contrast β (*b*) for the set-up of Fig. 11: $\phi_1 = 300$ μm (triangles), 200 μm (closed circles) and 100 μm (open circles).

$$2\mu^{-1}\sin(\theta_B)^2 < \Lambda_l, \tag{18}$$

μ^{-1} being the linear absorption length of the crystal and θ_B the Bragg angle. The first term in equation (18) is increasing rapidly with θ_B, so that the inequality is rarely fulfilled and only small Bragg indices and strongly absorbing samples have been studied in speckle dynamics experiments. In WAXS, like in Fig. 9, where the vicinity of a $(\frac{11}{22}\frac{1}{2})$ Bragg peak of the AuAgZn$_2$ alloy is studied, the value of β can be assumed constant because only a very small part of the reciprocal lattice is studied. In a symmetric Bragg-reflection configuration, the contrast due to the longitudinal coherence length can be estimated, in the case where the energy distribution of the monochromated beam is assumed to be a 'boxcar' function, close to the shape of the Darwin curve of a crystal. For a resolution in the vicinity of the Bragg Q_B value with a Bragg angle θ_B, $\delta q = 2\pi\delta\lambda/\lambda^2$, one defines $s = \mu/[\delta q \sin^2(\theta_B)]$ and the longitudinal β is

$$\beta_l = s[\arctan(2/s) - (s/4)\log(1 + 4/s^2)]. \tag{19}$$

For AuAgZn$_2$ (Fig. 9), $\beta_l \simeq 0.6$, and the transverse coherence of the set-up yields $\beta_t \simeq 0.2$. The product of these two terms corresponds to the observed β value of 0.1 in Fig. 10.

In the case of nanocrystals, μ^{-1} can be replaced by the crystal size in equation (18). As for (111) silicon monochromators, $\Lambda_l > 0.5$ µm, full coherence is easily achieved for submicrometric samples. For smaller sample sizes, monochromators with a larger bandwidth are also desirable here in order to compensate for low scattering cross sections.

In practice, for speckle measurements, reliable results are difficult to obtain with β smaller than a few percent. For 'lensless' imaging, the scattered intensity variations have to be accurately measured in order to be able to restore the phase and β should be much closer to unity.

4. Using speckles for the study of submicroscopic dynamics

The XPCS technique is devoted to the study of the dynamics of inhomogeneities. Many experimental results were obtained in soft condensed-matter systems and an overview of the results can be found in Grübel & Zontone (2004). A short summary of the results is given here and hard condensed-matter applications in alloys, quasicrystals *etc.* are described.

4.1. Fluctuations in dilute systems

One first experiment was the observation of the fluctuations of colloid gold particles by Dierker *et al.* (1995). For isolated and non-interacting particles, like the Brownian motion of latex spheres of radius R in a liquid, the function $g^{(2)}$ can be written as

$$g^{(2)}(q, t) = \exp -2q^2 \langle r^2(t) \rangle. \tag{20}$$

In Mochrie *et al.* (2003) and Lumma, Lurio, Borthwick *et al.* (2000), polystyrene spheres in glycerol were studied. Einstein's classical law (Einstein, 1906; Uhlenbeck & Ornstein, 1930) for particle diffusion in a liquid was first

observed in the case of spheres in the limit of low volume fraction f_v:

$$\langle r^2(t) \rangle = D_0 t = k_B T t/(6\pi\eta R_h), \tag{21}$$

where η is the viscosity and R_h is the hydrodynamic radius, *i.e.* the sphere radius R here. To summarize, the dynamic behavior

$$g^{(2)}(q, t) = \exp -2t/\tau(q), \tag{22}$$

with the equation

$$\tau(q) = (D_0 q)^{-2}, \tag{23}$$

is the signature of classical Brownian motion. This behavior was observed in the case of palladium colloidal particles, but the estimate of R_h in equation (21) showed large colloidal-particle agglomeration, probably connected to radiation damage (Thurn-Albrecht *et al.*, 1996). In the case of fractal colloidal palladium particles, a slowing down was observed when these overlap for $f_v = 0.008$. The value of D was found to decrease by a factor of three for this volume fraction as compared to the dilute case, although this system remained essentially Brownian (Thurn-Albrecht *et al.*, 1999).

4.2. Concentrated systems

For concentrated colloidal systems, the SAXS spectrum shows a peaked correlation function $S(q)$ for $qR \approx 2$. For these systems, XPCS is a very useful tool because they are opaque or they exhibit strong multiple scattering for DLS and also because XPCS provides measurements in the q domain $1 < qR < 5$ for $R < 0.1$ µm. In this region, the model equation (23) is not valid, as was first observed from measurements on block copolymer micelles (Mochrie *et al.*, 1997). When micelles were spherical, the results were fitted with a simple exponential [equation (22)], but the estimate of $D = [\tau(q)q^2]^{-1}$ showed a q dependence similar to that of $S(q)$.

In the case of concentrated latex particles in liquids (Lumma, Lurio, Borthwick *et al.*, 2000), $g^{(2)}(q, t)$ did not have a simple exponential behavior. From the linear shape of $\ln[g^{(2)}(q, t)]$ for short and long times, a short time D_s and a long time D_L diffusion constant could be obtained, different from D_0 calculated from equation (21). The qR and f_v variations of D_0/D_s showed a behavior similar to $S(q)$ for $0.13 < f_v < 0.52$ and $1 < qR < 7$. The static $S(q)$ and the dynamic D_0/D_s results were in agreement with the hard-sphere model and with the simulations of Beenakker & Mazur (1984). The dynamics of the fluctuations is strongly modified by the 'cage effect' (Grübel *et al.*, 2000). For latex particles, the stabilization of the structure is essentially steric.

In charged colloidal suspensions, the hard-sphere model cannot be used (Grübel *et al.*, 2000) for $S(q)$. For the study of the dynamics, the hydrodynamic function $H(q) = D_s(q, f_v)S(q)/D_0$ was introduced. This ratio is unity with no hydrodynamic interactions. It is independent of the model for the correlation function $S(q)$ and Beenakker & Mazur (1984) have given its qR and f_v dependence in the case of long-range hydrodynamic interactions. This approximation was questioned by studying charged colloidal suspension (Riese *et al.*,

2000). Non-deionized and deionized silica spheres in a water–glycerol mixture ($f_v = 0.089$) were compared. The deionized sample showed a significant discrepancy with the long-range hydrodynamics interactions. This corresponds to hydrodynamic screening, which has been connected to the strong Coulomb interactions in the deionized system.

This hydrodynamic interaction is an important parameter in the sedimentation problem.

One interesting possibility of XPCS is that one carries out *in situ* experiments. In the case of magnetic colloids (Wagner *et al.*, 2005; Robert *et al.*, 2005), a magnetic field orders the particles (Wiedenmann & Heinemann, 2005) and the diffusion process of the magnetic particles becomes anisotropic (Lal *et al.*, 2001).

4.3. Fluctuations in liquids

The dynamics of the critical fluctuations was addressed in the case of the consolute point of the binary hexane–nitrobenzene mixture, which can be considered as a model system for phase transitions with a 'conserved order parameter' [model *B* in Hohenberg & Halperin (1977)]. Dynamical measurements were carried out in the vicinity of $T_c \simeq 292$ K with a pink beam and a point detector, and the precision available from the measurements was carefully discussed (Dufresne *et al.*, 2002). These experiments were performed for $0.003 > q > 0.001$ Å^{-1}, corresponding to a region of DLS experiments (Chen *et al.*, 1983).

Capillary waves at the surface of liquids can be observed in a grazing-incidence scattering experiment, where the incident angle $\theta_i < \theta_c$. Capillary waves are detected in the directions of **q** parallel to the surface $q_\parallel$, which means asymmetric measurements, the exit angle θ_f being larger than θ_i. The variations of the speckle contrast with θ_f was discussed in Madsen *et al.* (2005). At the liquid surface, capillary waves can be oscillatory if the damping due to viscosity can be neglected and 'overdamped' for large viscosity. This latter behavior was first identified in the case of pure glycerol (Seydel *et al.*, 2001), where the correlation function $g^{(2)}(t)$ was exponential. The dispersion law for overdamped capillary waves $\tau = \eta/(\pi\sigma_s q)$, with σ_s the surface tension, was valid. For low viscosity, an oscillatory behavior, of frequency ω, is expected, with the dispersion relation $\omega = q^{3/2}(\sigma_s/\rho)^{1/2}$, where ρ is the density of the liquid. For pure water, the capillary waves can be observed only for ($q_\parallel \simeq 5 \times 10^{-6}$ Å^{-1}), where their ω becomes low enough ($\omega \simeq 10^5$ s^{-1}) for XPCS (see Fig. 1). As experiments were carried out very close to the tails of the specular reflection due to the surface (Gutt *et al.*, 2003), heterodyning was observed between the amplitude of the specular reflection and that of the capillary waves. In this case, the heterodyne function $g^{(1)}$ is written

$$g^{(1)}(q_\parallel, t) = \exp(-t/\tau)\cos(\omega t), \qquad (24)$$

and the oscillatory terms, which should vanish in $g^{(2)}$, were observed. The predicted dispersion relation $\omega \propto q_\parallel^{3/2}$ was valid. In a water–glycerol mixture of suitably chosen concentration, the transition from the high-temperature oscillatory

behavior (at 303 K) to the overdamped one (at 278 K) was observed (Madsen *et al.*, 2004).

In smectic membranes, for thicknesses l in the 10 µm range, the simplified law $\tau \propto l$ was observed (Price *et al.*, 1999). Results were obtained for **q** at a Bragg position, in the specular direction, yielding a large intensity and reliable results were obtained for correlation times of 0.1 µs (Sikharulidze *et al.*, 2002). These results could be compared to neutron spin-echo measurements for thick membranes (Sikharulidze *et al.*, 2003), with an overlap in the fluctuation time ranges but for different scattering vectors. For thinner layers, oscillating behaviors were observed, corresponding to collective membrane oscillations (Fera *et al.*, 2000; Sikharulidze *et al.*, 2002). In Sikharulidze *et al.* (2003), it was noticed that, for the regime where τ was $q_\parallel$ independent, its estimated value decreased by a factor of two when $q_\parallel$ was increased from zero (the Bragg peak position) to 3.5×10^{-4} Å^{-1}. This clearly indicated the transition from heterodyning, where the function $g^{(1)}(t) = \exp(-t/\tau)$ is observed, to homodyning, where equation (22) is valid with a half-time exponential (Berne & Pecora, 2000). These experiments are discussed in detail in Sikharulidze *et al.* (2005) and Sikharulidze & de Jeu (2005).

Pure polymers have low scattering intensities and they are radiation sensitive, but XPCS could be used for measuring the viscosity of thin polymer films (Kim *et al.*, 2004). The thickness and the molecular-weight dependence of the relaxation was obtained (Li *et al.*, 2005).

4.4. Fluctuations in filled polymers

Transparent polymers have been extensively studied by DLS, but X-rays bring new insights in the domain of filled polymers. These are either opaque or strong multiple scatterers for light and transparent to X-rays. As filling particles (silica, carbon black) have a large SAXS intensity and as the fluctuations can be slow, measurements could be performed with low-intensity coherent beams, reducing radiation damage.

Filled polymers can have various kinematical behaviors, depending on the concentration and on the manufacturing process. In Geissler *et al.* (2000), the XPCS method was used for comparing liquid and thixotropic samples. In Fig. 14, the time evolution of three samples is shown for $q = 1.71 \times 10^{-3}$ Å^{-1}. In this figure, the $t = 0$ limit fixes $\beta \simeq 0.23$ and three very different time behaviors are observed: the 'liquid' sample has a fluctuation time of about 30 s, the 'thixotropic' sample has an observable fluctuation time of half an hour. These two samples are compared with a static sample, which provides a check of the experimental stability in the range of 1 h. In this experiment, the dynamics of the studied system was very slow, so that the experiment could be carried out at a beamline (BM2 of ESRF) of small intensity (about 10^6 photons s^{-1}) (Livet *et al.*, 1998). The set-up summarized in Fig. 11 was used for these measurements, but the pinhole (diameter $\phi = 10$ µm) was circular and guard slits were set close to the sample, 0.2 m after the circular pinhole.

Silica gels in liquid crystals provide information on the dynamics of the fluctuations in the vicinity of a second-order transition. In this case, critical slowing down can be observed. Retsch *et al.* (2002) have fitted $g^{(2)}$ with a modified exponential behavior:

$$g^{(2)}(q, t) = \exp -2[t/\tau(q)]^{\mu}. \qquad (25)$$

This equation corresponds to 'anomalous diffusion processes' (Bouchaud & George, 1990). It is called 'stretched' (Krall & Weitz, 1998) for $\mu < 1$ and 'compressed' for $\mu > 1$ (Cipelletti *et al.*, 2000). The exponent μ can vary from 0 to 2 for the process to be a stationary and ergodic 'stable Lévy flight'. In practice, this equation is mainly used for non-ergodic systems. A review of its applications to viscoelastic systems is given in Scheffold & Schurtenberger (2003) and all light scattering measurements can be extended to X-rays. In the case of samples exhibiting long-term relaxations, like 'jamming systems' (Cipelletti *et al.*, 2000), it may be difficult to distinguish in the correlations slow sample movements from random fluctuations: both can contribute to $\langle r(t)^2 \rangle$ in equation (20). These sample movements can be observed in XPCS by studying the drift of the speckle pattern in the detector. These are not observed in a DLS experiment because the size of the beam is millimetres. For the 10 μm beam sizes of XPCS, local flows can be observed.

Heterodyne detection of the fluctuations was used in order to distinguish in a rubber random fluctuations from the flowing occurring after stretch release (Livet *et al.*, 2006). The sample was an ethylene-propylene rubber filled with carbon black (volume fraction 20%). In transmission SAXS, the length e of the coherence volume in equation (9) can be of a few millimetres and heterodyning can be measured by simply stacking along the beam path a strongly scattering static aerosil and the fluctuating sample. For instance, Fig. 15 shows typical corre-

Figure 14
Correlations observed at $q = 1.71 \times 10^{-3}$ Å^{-1} with three samples: a 'liquid' (crosses), with a short fluctuation time, a 'thixotropic' sample (open circles) exhibiting long-time fluctuations and a static aerogel (closed circles) for a test of the experimental stability. From Geissler *et al.* (2000).

lations obtained. Strong oscillations are observed due to the interferences between the reference and a moving rubber. These oscillations could be described with the heterodyne contribution [see equation (24)]

$$\gamma(q, t) \simeq 1 + \beta_1 + \beta_2 \exp -[t/\tau(q)]^{\mu} \cos(\omega t) + \ldots, \qquad (26)$$

as plotted in Fig. 15. Except for the larger q values, the time variations are dominated by an oscillating behavior, characteristic of the drift of the sample. The drift velocity v is connected to the value of ω, to q and to the angle ϕ between the direction of the drift and the direction of **q** (see Berne & Pecora, 2000, p. 79): $\omega = qv \cos(\phi)$. In the case of Fig. 15, this velocity is $v = 15$ Å s^{-1}.

For this system, similar to 'jammed' systems, the local character of the X-ray measurements and the precise measurement of extremely small velocities can yield new insights into the 'mesoscopic' processes occurring. Another advantage of heterodyning is that the irradiation of the sample can be significantly reduced if the beam that has crossed the static reference still gives a reasonable experimental SNR. This heterodyning method should also be useful for microrheology studies, like in Papagiannopoulos *et al.* (2005).

4.5. Fluctuations in metals

The first speckle measurements consisted of observing the ordering peak of a Cu_3Au single crystal (Sutton *et al.*, 1991), and the first observation of critical fluctuations in an ordering system (the Fe_3Al Heussler transition) was reported in Brauer *et al.* (1995).

Quasicrystals are condensed-matter systems of high symmetry (Shechtman *et al.*, 1984) and they have long-wavelength distortion modes called 'phasons', which induce a strong anisotropic scattering in the vicinity of the Bragg peaks (Coddens *et al.*, 1991). First, at room temperature, a permanent speckle structure was observed in the region of phason diffuse scattering, showing the stability of the phasons at this temperature (Létoublon *et al.*, 2001). Then *in situ* studies were carried out at high temperature and time-dependent phason fluctuations were observed above 873 K (Francoual *et al.*, 2003). In Francoual *et al.* (2006), the dynamics of the phason fluctuations was shown to be of a diffusive type, with a diffusion constant $D_{\perp}$ like in equation (23) and a q^{-2} dependence of the fluctuation time τ calculated from equation (22).

Charge-density waves (CDW) are observed from Bragg peaks in metals. They form a well ordered pattern, with very thin Bragg peaks, at least for the scale explored in XIFS, like in the $NbSe_3$ system. In Sutton *et al.* (2002), only a small number of speckles were observed and applying an electric field induced CDW sliding. For systems exhibiting a nearly monodomain region of CDW ($K_{0.3}MoO_3$), by exploring the sample, individual CDW dislocations could be observed (Le Bolloc'h *et al.*, 2005).

4.6. Dynamics of phase transitions

The dynamics of the irreversible process of a phase transition could be studied in speckle experiments. After quenching
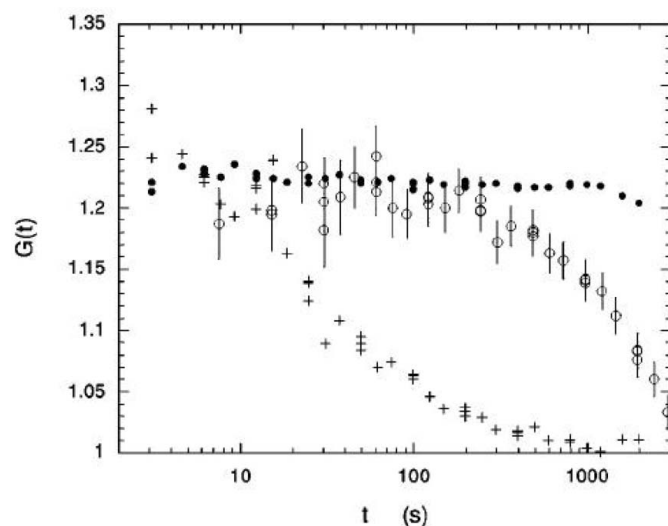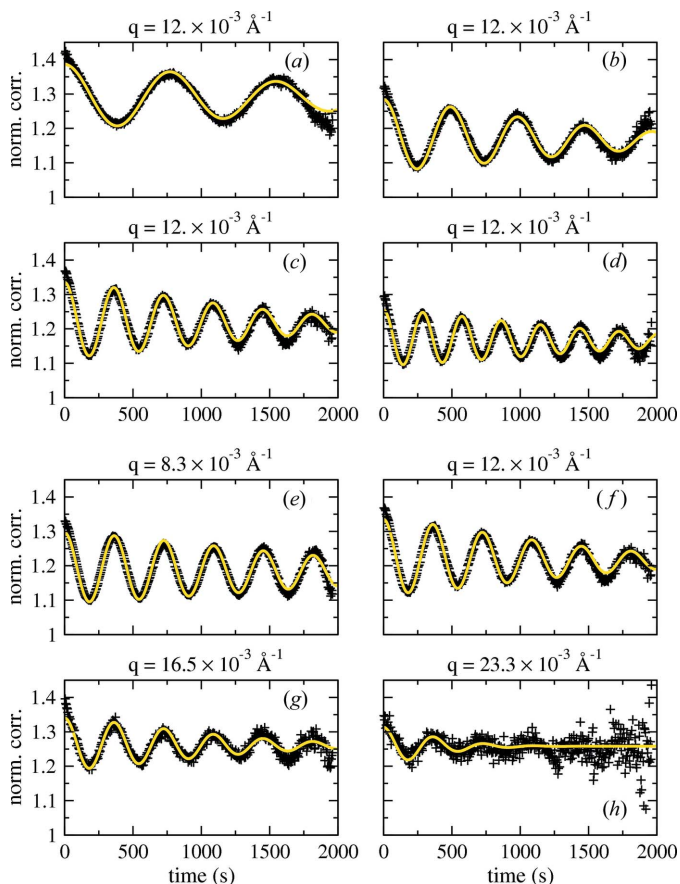
of a sample, the time evolution of the speckle structure can be followed. In a classical (incoherent) experiment, a quasi-stationary process can be defined from a dynamic size evolution $\mathcal{L}(t)$, which increases with time as t^n. This average size is the main relevant parameter. Two different dynamics can be defined from Hohenberg & Halperin (1977), depending on whether the order parameter is conserved (model B, n = 1/3), like in the unmixing of alloys, or not (model A, n = 1/2), like in ordering transitions.

For both dynamics, the time evolution of the speckle structure reflects the lack of time invariance due to the initial quench of the sample [non-ergodicity in equation (13)]. For a comparison with a stationary process, the measured intensity is normalized by the incoherent intensity corresponding to the same time t, estimated from an average over $\mathbf{q}$:

$$D(\mathbf{q}, t) = I(\mathbf{q}, t)/\langle I(\mathbf{q}, t)\rangle_{\mathbf{q}} - 1. \quad (27)$$

Fig. 16 shows the time evolution of $D(\mathbf{q}, t)$ obtained in a SAXS experiment during unmixing of an Al–Li sample (Livet et al., 2001) for a set of pixels of the same $|\mathbf{q}|$ value. The increasing

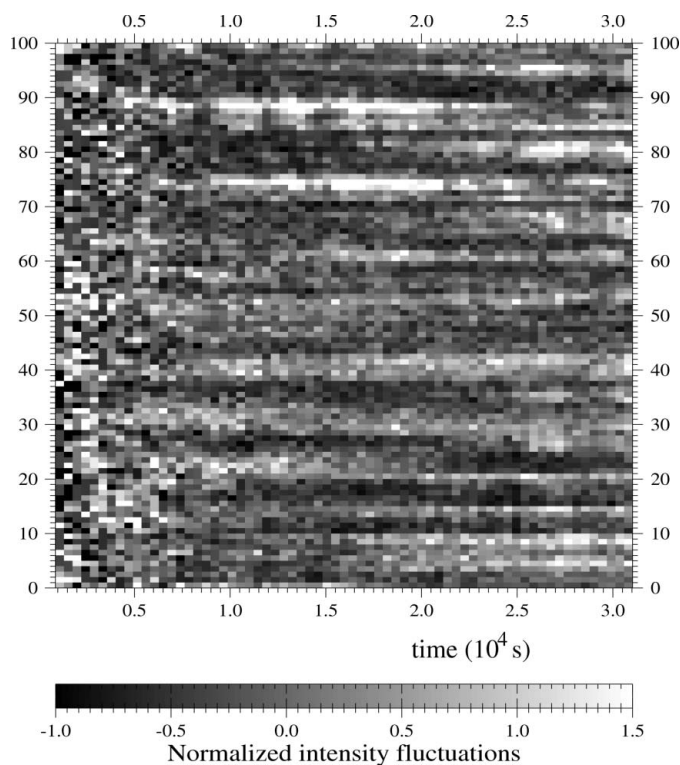persistence of the pixel pattern with aging time is clearly visible.

The modeling of the time evolution of the speckle structure was obtained from two-dimensional simulations: Brown et al. (1997) for the A model and Brown et al. (1999) for the B model. The two-time correlation (Sutton et al., 2003)

$$C(q, t_1, t_2) = \langle D(\mathbf{q}, t_1)D(\mathbf{q}, t_1)\rangle_{\mathbf{q}} \quad (28)$$

was introduced.

Experiments were performed in model A: phase separation in a sodium borosilicate glass (Malik et al., 1998) and in Al–Li (Livet et al., 2001); and in model B: ordering in Cu–Pd (Ludwig et al., 2005) and in Cu_3Au (Fluerasu et al., 2005). All showed that the speckles in the high-intensity region had a fluctuation time of the order of the aging time. For a long enough time, or for asymptotic intensity, a cross over to a $t^{2/(n+1)}$ behavior corresponding to the observation of fluctuations of the interfaces between the two phases could be observed.

Another method for the study of the dynamics of phase transitions was proposed by Weinkamer & Fratzl (2003). For the problem of the dynamics of the unmixing of alloys, i.e. model B, two microscopic models for the size increase of the precipitates can be distinguished: the evaporation–condensation model [called LSW (Lifshitz & Slyozov, 1961; Wagner, 1961)], where atoms migrate from smaller precipitates to larger ones, and the coagulation model, where precipitates grow by fusion. Simulations by the Monte Carlo method

Figure 15
Heterodyne correlations obtained from the CL-EPR sample. (a)–(d) Various values of the $\mathbf{q}$ projections $[q\cos(\phi) = 0.569, 0.899, 1.21$ and 1.52×10^{-3} Å$^{-1}]$ along $\mathbf{v}$ for $q = 12 \times 10^{-3}$ Å^{-1}. (e)–(h) Various q values for $q\cos(\phi) = 1.21 \times 10^{-3}$ Å^{-1} showing the identical period of the oscillations. Continuous curves correspond to fits with equation (26). From Livet et al. (2006).

Figure 16
Time evolution of normalized intensity fluctuations at $q = 0.0117$ Å^{-1} [equation (27)] showing the increasing persistence of the speckle structure after quench of an Al–Li sample. From Livet et al. (2001).

showed that these two models gave different shapes of the time evolution of the speckle patterns. This feature can be connected to the differences between the slow growth of the inclusions in the first model, where a regular flow of individual atoms agglomerates on the precipitates, and the sudden rare and large changes induced by the coagulation of large precipitates. This needs a careful examination of the statistics of the fluctuations in the measured time series.

Various methods for the study of these time fluctuations were used for the problem of growing precipitates (Stadler *et al.*, 2003, 2005). Comparing two model systems, these authors concluded that the decomposition of the Al–Ag alloy followed the LSW process and Al–Zn the coagulation one. This method was extended to ordering systems (model *A*) (Stadler *et al.*, 2004).

These measurements could be carried out in a short time relative to the global aging of the system. By this method, a complete history of the speckle structure does not have to be recorded. This type of interpretation seems well adapted to non-ergodic systems.

5. Imaging

The possibility of imaging a real-space object from the measurement of the coherent scattered intensity is based on oversampling in the reciprocal space. From precise measurements of the modulus of the object Fourier transform (FT), the phase and the amplitude of the real object have to be obtained. This needs oversampling by at least a factor of two as compared with the Nyquist sampling theorem, which states $\delta q = 2\pi/\mathcal{D}$, where $\mathcal{D}$ is the sample size.

The basic algorithms are iterative Fourier transforms between estimates $G_k(\mathbf{q})$ of the scattering amplitude $A(\mathbf{q})$ in the reciprocal space and estimates $g_k(\mathbf{r})$ of $a(\mathbf{r})$ in the real space, where k refers to the kth cycle. Constraints are added in order that the calculation converges towards the solution.

The main constraint in the reciprocal space is that the modulus of the estimation of the amplitude in the reciprocal lattice is $[I(\mathbf{q})]^{1/2}$, which means that at each cycle $G_k(\mathbf{q})$ is replaced by $G'_k(\mathbf{q}) = [I(\mathbf{q})]^{1/2} \exp[i\Phi(G_k(\mathbf{q}))]$, where $\Phi(G_k(\mathbf{q}))$ is the phase of G_k, wherever the intensity has been measured. In real space, the constraint is that of a finite support, which can be adjusted during cycling. This support must agree with the oversampling condition but, the higher the oversampling, the easier the convergence (Miao *et al.*, 1998). This is the Gerchberg–Saxton algorithm, also called error reduction (ER) (Gerchberg & Saxton, 1972). This algorithm is usually combined with the hybrid input–output (HIO) algorithm of Fienup (1982), where the finite support constraint is relaxed. The constraint of real and positive $a(\mathbf{r})$ is also often used in astronomy and in imaging problems.

An excellent description of the sampling problems can be found in van der Veen & Pfeiffer (2004). Many simulations based on these algorithms have been published in order to discuss the need for oversampling (Miao *et al.*, 1998; Mielenz, 1999) or the influence of experimental noise on the resulting object image (Marchesini, He *et al.*, 2003).

This technique was first tested on very simple strongly scattering objects like a two-dimensional pattern of gold dots (Miao *et al.*, 1999). The soft X-ray scattering was recorded with BI-CCDs and the resolution was of the order of tens of nanometres. Simple well prepared objects were studied (He, Marchesini, Howells, Weierstall, Chapman *et al.*, 2003) and the reconstructed image could be compared with scanning-electron-microscopy images (He, Marchesini, Howells, Weierstall, Hembree & Spence, 2003). These first experiments were carried out on two-dimensional samples prepared with 100 nm diameter gold balls on an SiN window. The samples were studied in transmission and various methods were used to compensate for lack of measurements in the beam stop.

In He, Marchesini, Howells, Weierstall, Hembree & Spence (2003), the Patterson function (PF) was calculated by carrying out a FT of the measured spectrum. This function is the autocorrelation of the electron density of the sample and, from the properties of the convolution products, with well separated clusters, direct information on the distance between clusters was obtained from the observation of the PF. For a cluster well separated from a single gold ball, the shape of the cluster could be obtained. This property was systematically used by Eisebitt, Lörgen *et al.* (2004), where the scattering of a hole and a well separated sample was measured. As the two amplitudes coherently interfered, the PF directly gives the sample shape as the convolution of a point hole (a Dirac distribution) and the sample.

This holographic method using heterodyning between the scattering of a point source and the sample was applied to the study of the magnetic map of a Pt–Co multilayer. Magnetic scattering is observed in the vicinity of the L_{III} edge of transition metals (Menteş *et al.*, 2002; Chesnel *et al.*, 2002), which can be controlled by tuning the energy and the polarization of the soft X-ray beam. In Eisebitt, Lüning *et al.* (2004), a hologram is measured between a hole and a distant sample and only a single Fourier transform is necessary to obtain an image of the magnetic configuration. The image resulting from the Fourier inversion was successfully compared with magnetic force microscopy measurements. Another method used was to illuminate the sample with the reference wave of a well defined 2.5 μm pinhole (Eisebitt *et al.*, 2003, 2005) and to observe the changes in magnetic scattering with X-ray energy and polarization.

The magnetic configuration of multilayers was also studied in the symmetric Laue reflection configuration and speckles were used in order to image the configurational changes obtained by applying a magnetic field (Chesnel, Belakhovsky *et al.*, 2004; Chesnel, van der Laan *et al.*, 2004; Deutsch & Mai, 2005).

Except for magnetic measurements, first experiments used soft X-rays because for wavelengths larger than 1 nm the number of photons per coherence area is larger, and also because the resolution requirements were lower (Sayre *et al.*, 1998). First two-dimensional reconstructions were obtained with fixed samples and area detectors. The samples were studied in transmission and various methods were used to compensate for the lack of measurements in the beam stop.
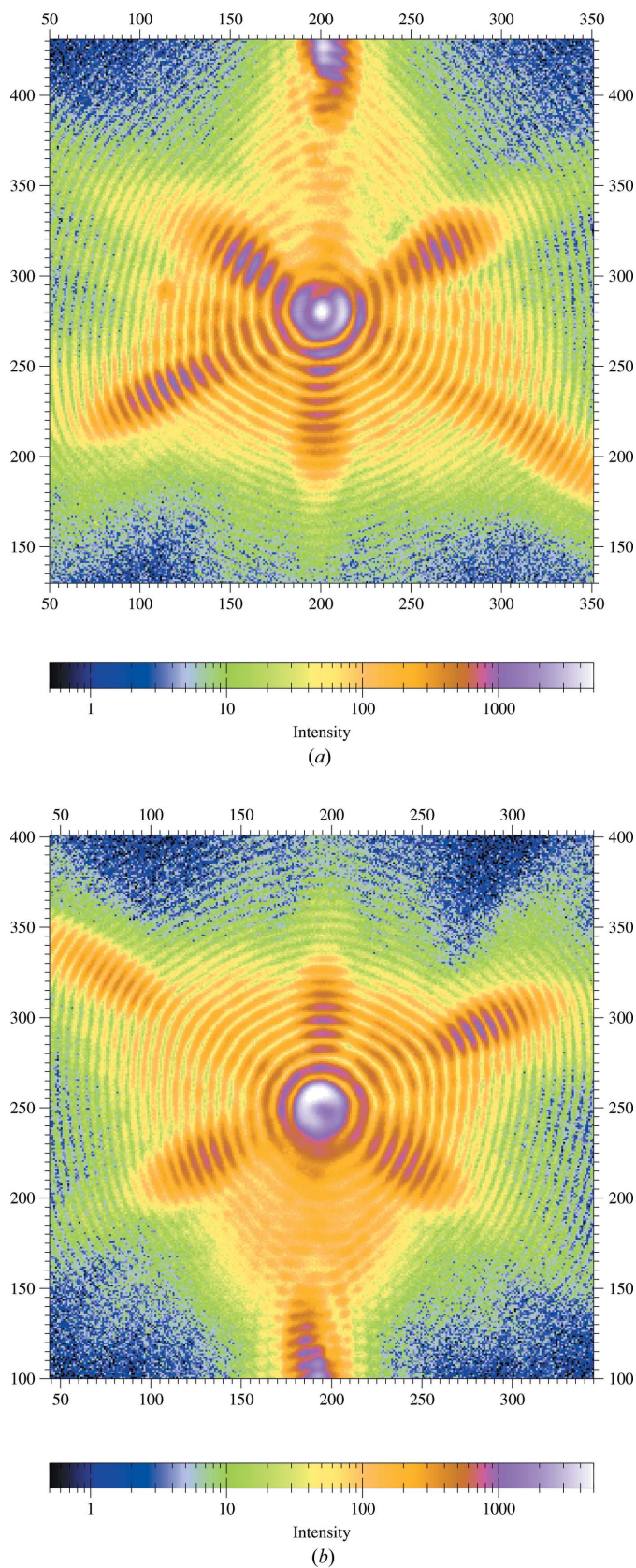
Figure 17
Diffraction from a 1 µm gold crystal measured on both sides of the center of a (111) Bragg peak, showing the high-precision central symmetry of the scattering: $\lambda = 1.55$ Å, sample-to-detector distance 0.87 m, pixel size 22 µm. Results from ID01 at the ESRF.

Obviously, samples were very thin and it was difficult to study three-dimensional systems, which are thicker. For buried structures (Miao *et al.*, 2002), the three-dimensional **q** space was sampled by a reduced set of two-dimensional diffraction patterns and short wavelengths ($\lambda = 2$ Å) from an Si_{111} monochromator were used. For the large number of three-dimensional **q** values that were not measured, no constraint was imposed on the modulus. For systems with a limited number of different layers, like a set of metallic patterns buried close to the surface of a silicon wafer, the three-dimensional image was well reconstructed. This technique was extended to the study of gold particles deposited at the surface of an SiN pyramidal membrane (Marchesini, Chapman *et al.*, 2003). As these particles were deposited on a (non-planar) surface, the full sampling of the three-dimensional **q** space was not necessary. These measurements need the development of new set-ups of high reliability in order to position and to rotate the samples. One can observe in passing that recently developed set-ups use many tools (sample holders, cryo holder, ...) from electron-microscope techniques (Beetz *et al.*, 2005). Techniques are developed for solving the inversion problem with blank parts in the scattering planes. An excellent summary of the method is found in Chapman *et al.* (2006)

6. Nanocrystals

Imaging of crystals and of defects in crystals is an essential capability of X-rays and this is achieved in the vicinity of Bragg peaks. First results were also obtained in gold particles. This metal is not oxidized in air and it has a large atomic coherent X-ray cross section ($\propto Z^2$). By dewetting a thin metallic film, small crystals can be obtained. Their Bragg scattering was measured and the diffraction corresponding to an individual crystal was selected by Robinson *et al.* (2001) and a combination of ER and HIO algorithms was used. In the case of two-dimensional measurement, only the particle-shape projection can be obtained but the general crystal shape and some facets of the gold crystals were visible. For a perfect crystal, the intensities in the vicinity of a Bragg peak should be symmetrical about the center of the Bragg peak. In the case of asymmetric scattering, corresponding to an imaginary part of the electron density, a strain field has been introduced for simulations (Robinson & Vartanyans, 2001) in a way similar to that of Huang scattering. The first-order term of the amplitude is given by

$$
\begin{aligned}
A(\mathbf{q}) &= \sum_R \rho(\mathbf{R}) \exp i\mathbf{q}[\mathbf{R} + \mathbf{u}(\mathbf{R})] \\
&\simeq \sum_R \rho(\mathbf{R})[1 + i\mathbf{G}\mathbf{u}(\mathbf{R})] \exp i\mathbf{q}\mathbf{R},
\end{aligned} \tag{29}
$$

where **G** is the Bragg vector. This means that the imaginary part in the electron density $\rho'(\mathbf{R})$ corresponds to a crystal distortion: $\rho'(\mathbf{R}) = \rho(\mathbf{R})\mathbf{G}\mathbf{u}(\mathbf{R})$. This approximation assumes that $\mathbf{u}(\mathbf{R}) \ll a$, where a is the lattice parameter. It is thus difficult to use for defects with large and sudden phase jumps, like dislocations, twinning or stacking faults, but it may be valid for surface-stressed nanocrystals.

The measurements were extended to the three-dimensional space. In this case, the area detector can be considered as planar and rotating the sample gives measurements in a set of nearly parallel planes. For samples with a strain field due to residual defects, many planes in the third dimension have to be measured, corresponding to the continuous function $\mathbf{u}(\mathbf{R})$.

First three-dimensional reconstructions of the shape of Au crystals of dimensions in the μm range (Williams *et al.*, 2003, 2006) assumed $\rho(\mathbf{R})$ to be real and positive: at the end of each cycle k, the complex function $\rho_k(\mathbf{R})$ was projected onto the real axis and was set to zero if negative. A maximum of this function close to the center of the gold crystal was interpreted as an artifact due to partial beam coherence. The result also showed regions of zero intensity parallel to (111) planes which were attributed to twinning.

For X-rays in the 8 keV range and crystals of heavy metals like gold or lead, the extinction length t is of the order of 1 μm for the (111) Bragg peak of the f.c.c. lattice. As the use of the dynamical theory seems very difficult, this technique is devoted to the study of submicrometric crystals. For such small samples, the beam must be focused. This reduces the coherence volume and this can also induce phase distortions. For μm beam sizes, Robinson *et al.* (2003) have calculated the modification of the scattering for non-plane waves. As all FT calculations assume plane waves, it seems to be of the highest importance to verify this condition in an experiment.

For instance, the focusing set-up of the ID01 beamline of the ESRF was used for the diffraction of micrometric gold crystals, and the symmetry of the scattering could be checked with a high precision. Fig. 17 shows the details of the measured diffraction in two (nearly) symmetrical positions of the sample relative to the center of the (111) Bragg peak of the crystal. These two images were obtained from 1000 frames of 1 s each after having used the droplet algorithm (Livet *et al.*, 2000). In this case, observing a symmetric pattern means that the crystal can be considered as perfect and that only the crystal boundaries have to be calculated, and measuring a large number of diffracting planes similar to Fig. 17 can become unnecessary because the function $\rho(\mathbf{R})$ could be assumed constant.

The reconstruction of the shape of samples in all techniques requires a high degree of coherence, as discussed in Vartanyants & Robinson (2001). Since Bates (1982) and Millane (1996), one considers that large enough oversampling, high enough coherence and precise enough measurements should yield a unique inverse solution in the two-dimensional and the three-dimensional spaces, but 'stagnation' can be observed. Stagnation seems to be less of a problem in three-dimensional than in two-dimensional reconstruction (Williams *et al.*, 2006). The problem has been compared with statistical physics, where the solution is a 'fixed point' and the stagnation corresponds to 'strange attractors' (Elser, 2003). A summary of some results is found in Robinson & Miao (2004).

The most recent example of a crystal image reconstruction can be found in Pfeifer *et al.* (2006), where the shape and the strain field of a small lead monocrystal of 0.75 μm diameter was determined.

7. Discussion

The number of applications of coherent scattering is increasing rapidly, as well as the number of available sources and of new set-ups able to carry out such measurements. These are essentially connected to the availability of synchrotrons of lower energy in the 2–3 GeV range, taking advantage of the improvements of the insertion devices (undulators) that have a high brilliance in the 500–12 000 eV range. For the techniques already available and for sources becoming operational in the near future, reasonable improvements for speckle dynamics may be expected.

First, for the incoming beam, the maximum value of the product βI (the 'beamline quality') corresponds to the available coherent flux given by equation (6). For a source like the ID10 undulators of ESRF, the estimate of this product is close to 10^{11} photons s^{-1} for $\delta\lambda/\lambda \simeq 1.4 \times 10^{-4}$, and the observed intensity is of the order of a few 10^9 photons s^{-1} with $\beta \simeq 0.2$. This is a loss of two orders of magnitude occasioned by the set-up of this experiment. In Abernathy *et al.* (1998), the origin of the losses is briefly discussed, and beamline improvements are in progress. These are difficult to achieve if the beamline is not dedicated to coherent scattering. With modern optics, large β values are obtained, even for XPCS, and, for the same βI, the sample irradiation can be reduced. Such a beamline needs high stability and high-quality optic elements optimized for small beam sizes (less than 300 μm), which means low total heat load in optics. These needs are somewhat contradictory with the specification of a general use beamline.

Second, the fact that there is no intermediate detection method between submicrosecond time resolution with a point detector and fractions of seconds with a CCD constitutes a gap that could be partly filled by faster reading of the CCDs used for this type of experiment. Apart from attempts to develop fast CCD readings (Falus *et al.*, 2004), pixel detectors with resolutions down to 55 μm (Pfeiffer *et al.*, 2004; Bisogni *et al.*, 2006) are very promising.

In imaging, the main activity is in the domain of submicrometric samples. The long-term development for this technique is the study of nanostructured samples like the buried interconnections in integrated circuits, the defects introduced by electromigration, the interfacial stresses, or the dewetting between a metal and its substrate. X-rays can be used as a technique complementary to electron microscopy for their penetration depth and also for their resonant scattering properties.

In practice, the resolution of the technique is directly connected to the largest q value where scattered intensity can be measured. This makes background reduction an important problem. The resolution can nevertheless be discussed from scaling considerations (Shen *et al.*, 2004). For a fixed sample size ϕ, the intensity has a q^{-4} behavior, which means that the resolution $\delta\phi$ scales as $I^{-1/4}$, *i.e.* as $\mathcal{B}^{-1/4}$ for equivalent optics. For three-dimensional imaging, the increase of the number of reciprocal planes would transform the 1/4 exponent to 1/5. For nanoparticles, the goal can be to observe their shape, with a constant ratio $\delta\phi/\phi$. One interesting problem here is the

equilibrium shape of nanocrystals when their size ϕ is reduced. In this case, the coherence volume can be reduced by focusing (smaller Λ_t) and by increasing the bandwidth (smaller Λ_l), increasing the intensity in the coherence volume by a factor ϕ^{-3}.

In this case, $\delta\phi$ scales as $\mathcal{B}^{-1}$ ($\mathcal{B}^{-1/2}$ for a three-dimensional object). Recent experiments claim $\delta\phi \simeq 10$ nm and it seems that this method does not need a particularly large increase of source brilliance but optics improvements and background reduction.

Owing to their short penetration depth and their sensitivity to magnetism, soft X-rays are a useful tool for the study of the dynamics at the surface and of the mechanisms of magnetic domain reversal.

Stable focusing and well controlled plane waves seem very important for future progress. The use of apertures before the sample for limiting the beam size in imaging experiments induces strong wave distortions at short distances, which make FT-based methods difficult to use. Wave distortions can also explain some of the asymmetries in the observed scattering: the phase variations of the incoming beam can have the same effect as the introduction of an imaginary component in the sample electron density of equation (29).

The future of X-ray coherent scattering with free electron laser (FEL) sources will modify the problem of obtaining a coherent beam, and new experiments will become accessible. One can here notice that the increase in beam intensity obtained by improving the focusing technique already makes the irradiation damage an important problem. First, small metallic crystals at the surface of an insulating substrate (*e.g.* crystalline silicon with a nanometre thick layer of silicon oxide) are removed by electric charges due to electron photoemission. Conducting substrates like graphite are now used, but they may produce parasitic scattering significantly larger than the sample signal. Second, submicrometric samples can be strongly heated by the beam. Third, radiation damage in biological molecules makes the projects of studying single large-scale molecules with FELs a difficult challenge. Radiation damage is measured in Howells *et al.* (2005) and the balance between the sample irradiation necessary for structure measurements and its destruction, discussed in Marchesini, Chapman *et al.* (2003) and Shen *et al.* (2004) can limit the effective resolution to about 10 nm.

New sources providing a larger brilliance ($\mathcal{B} \simeq 10^{22}$) like the energy recovery linac at CHESS (USA) and damping wigglers at PETRA III (Germany) can bring significant improvements in 'non-destructive' experiments.

References

Abernathy, D. L., Grübel, G., Brauer, S., McNulty, I., Stephenson, G. B., Mochrie, S. G. J., Sandy, A. R., Mulders, N. & Sutton, M. (1998). *J. Synchrotron Rad.* **5**, 37–47.

Attwood, D. T., Naulleau, P., Goldberg, K. A., Tejnil, E., Chang, C., Beguiristain, R., Batson, P., Bokor, J., Gullikson, E. M., Koike, M., Medecki, H. & Underwood, J. H. (1999). *IEEE J. Quantum Elec.* **35**, 709–720.

Bates, R. H. T. (1982). *Optik (Stuttgart)*, **61**, 247–262.

Beenakker, C. W. J. & Mazur, P. (1984). *Physica (Uttrecht)*, A**126**, 349–370.

Beetz, T., Howells, M., Jacobsen, C., Kao, C.-C., Kirz, J., Lima, E., Menteş, T., Miao, H., Sanchez-Hanke, C., Sayre, D. & Shapiro, D. (2005). *Nucl. Instrum. Methods A*, **545**, 459–468.

Bérar, J.-F., Blanquart, L., Boudet, N., Breugnon, P., Caillot, B., Clemens, J.-C., Delpierre, P., Koudobine, I., Mouget, C., Potheau, R. & Valin, I. (2002). *J. Appl. Cryst.* **35**, 471–476.

Berne, B. J. & Pecora, R. (2000). *Dynamic Light Scattering.* New York: Dover Publications.

Bilderback, D. H., Elleaume, P. & Weckert, E. (2005). *J. Phys. B: At. Mol. Opt. Phys.* **38**, S773–S797.

Bisogni, M. G., Cicalini, E., Guerra, A. D., Delogu, P., Carpentieri, C., Fantacci, M. E., Panetta, D., Quattrocchi, M., Rosso, V. & Stefanini, A. (2006). *Nuovo Cim.* **29**, 421–427.

Born, M. & Wolf, E. (1980). *Principles of Optics*, 6th ed. Oxford: Pergamon Press.

Bouchaud, J.-P. & George, A. (1990). *Phys. Rep.* **195**, 127–293.

Brauer, S., Stephenson, G. B., Sutton, M., Bruning, R., Dufresne, E., Mochrie, S. G. J., Grübel, G., Als-Nielsen, J. & Abernathy, D. L. (1995). *Phys. Rev. Lett.* **74**, 2010–2013.

Broennimann, C., Eikenberry, E. F., Henrich, B., Horisberger, R., Huelsen, G., Pohl, E., Schmitt, B., Schulze-Briese, C., Suzuki, M., Tomizaki, T., Toyokawa, H. & Wagner, A. (2006). *J. Synchrotron Rad.* **13**, 120–130.

Brown, G., Rikvold, P. A., Sutton, M. & Grant, M. (1997). *Phys. Rev. E*, **65**, 6601–6612.

Brown, G., Rikvold, P. A., Sutton, M. & Grant, M. (1999). *Phys. Rev. E*, **60**, 5151–5162.

Brown, W. (1993). Editor. *Dynamic Light Scattering*, ch. 2. Oxford Science Publications.

Chapman, H. N., Barty, A., Marchesini, S., Noy, A., Hau-Riege, S. P., Cui, C., Howells, M. R., Rosen, R., He, H., Spence, J. C. H., Weierstall, U., Beetz, T., Jacobsen, C. & Shapiro, D. (2006). *J. Opt. Soc. Am. A*, **23**, 1179–1199.

Chen, S.-H., Lai, C.-C., Rouch, J. & Tartaglia, P. (1983). *Phys. Rev. A*, **27**, 1086–1095.

Chesnel, K., Belakhovsky, M., van der Laan, G., Livet, F., Marty, A., Beutier, G., Collins, S. P. & Haznar, A. (2004). *Phys. Rev.* **70**, 180402.

Chesnel, K., Belakhovsky, M., Livet, F., Collins, S. P., van der Laan, G., Dhesi, S. S., Attané, J. P. & Marty, A. (2002). *Phys. Rev. B*, **66**, 172404.

Chesnel, K., van der Laan, G., Livet, F., Beutier, G., Marty, A., Belakhovsky, M., Haznar, A. & Collins, S. P. (2004). *J. Synchrotron Rad.* **11**, 469–475.

Cipelletti, L., Manley, S., Ball, R. C. & Weitz, D. A. (2000). *Phys. Rev. Lett.* **84**, 2275–2278.

Cippelletti, L. & Weitz, D. A. (1999). *Rev. Sci. Instrum.* **70**, 3214–3221.

Cloetens, P., Barrett, R., Baruchel, J., Guigay, J.-P. & Schlenker, M. (1996). *J. Phys. D*, **29**, 133–146.

Coddens, G., Bellissent, R., Calvayrac, Y. & Ambroise, J.-P. (1991). *Europhys. Lett.* **16**, 271.

David, C., Nöhammer, B., Ziegler, E. & Hignette, O. (2001). *Proc. SPIE*, **4499**, 96–104.

David, C., Weitkamp, T., Nöhammer, B. & van der Veen, J.-F. (2004). *Spectrochim. Acta B*, **59**, 1505–1510.

Delpierre, P., Bérar, J.-F., Blanquart, L., Caillot, B., Clemens, J. C. & Mouget, C. (2001). *IEEE Trans. Nucl. Sci.* **48–4**, 987–991.

Deutsch, J. M. & Mai, T. (2005). *Phys. Rev. E*, **72**, 016115.

Dierker, S., Pindak, R., Fleming, R., Robinson, I. & Berman, L. (1995). *Phys. Rev. Lett.* **75**, 449.

Dufresne, E. M., Nurushev, T., Clarke, R. & Dierker, S. B. (2002). *Phys. Rev. E*, **65**, 061507.

Einstein, A. (1906). *Ann. Phys.* **19**, 371–381.

Eisebitt, S., Lörgen, M., Eberhardt, W., Lüning, J., Andrews, S. & Stöhr, J. (2004). *Appl. Phys. Lett.* **84**, 3373–3375.

Eisebitt, S., Lörgen, M., Eberhardt, W., Lüning, J. & Stöh, J. (2005). *Appl. Phys.* **A80**, 921–927.

Eisebitt, S., Lörgen, M., Eberhardt, W., Lüning, J., Stöhr, J., Rettner, C. T., Hellwig, O., Fullerton, E. E. & Denbeaux, G. (2003). *Phys. Rev. B*, **68**, 104419.

Eisebitt, S., Lüning, J., Schlotter, W. F., Lorgen, M., Hellwig, O., Eberhardt, W. & Stöhr, J. (2004). *Nature (London)*, **432**, 885–888.

Elser, V. (2003). *J. Opt. Soc. Am.* **20**, 40–55.

Fabrizio, E. D., Romanato, F., Gentil, M., Cabrini, S., Kaulich, B., Susini, J. & Barett, R. (1999). *Nature (London)*, **401**, 895–898.

Falus, P., Borthwick, M. & Mochrie, S. (2004). *Rev. Sci. Instrum.* **75**, 4383–4400.

Falus, P., Lurio, L. B. & Mochrie, S. G. J. (2006). *J. Synchrotron Rad.* **13**, 253–259.

Fera, A., Dolbnya, I. P., Grübel, G., Muller, H. G., Ostrovskii, B. I., Shalaginov, A. N. & de Jeu, W. H. (2000). *Phys. Rev. Lett.* **85**, 2316–2319.

Fienup, J. R. (1982). *Appl. Opt.* **21**, 2758–2768.

Fienup, J. R. (1987). *J. Opt. Soc. Am.* **A4**, 118–123.

Fluerasu, A., Sutton, M. & Dufresne, E. (2005). *Phys. Rev. Lett.* **94**, 055501.

Francoual, S., Livet, F., de Boissieu, M., Yakhou, F., Bley, F., Létoublon, A., Caudron, R. & Gastaldi, J. (2003). *Phys. Rev. Lett.* **91**, 225501.

Francoual, S., Livet, F., de Boissieu, M., Yakhou, F., Bley, F., Letoublon, A., Caudron, R., Gastaldi, J. & Currat, R. (2006). *Philos. Mag.* **86**, 1029–1035.

Gabor, D., Kock, W. E. & Stroke, G. W. (1971). *Science*, **173**, 11–23.

Geissler, E., Hecht, A. M., Rochas, C., Bley, F., Livet, F. & Sutton, M. (2000). *Phys. Rev. E*, **62**, 8308–8313.

Gerchberg, R. W. & Saxton, W. O. (1972). *Optik (Stuttgart)*, **35**, 237–246.

Grübel, G., Abernathy, D. L., Riese, D. O., Vos, W. L. & Wegdam, G. H. (2000). *J. Appl. Cryst.* **33**, 424–427.

Grübel, G. & Zontone, F. (2004). *J. Alloys Compd.* **362**, 3–11.

Gutt, C., Ghaderi, T., Madsen, A., Seydel, T., Tolan, M., Sprung, M., Grübel, G. & Sinha, S. K. (2003). *Phys. Rev. Lett.* **91**, 076104.

Hara, T., Yabashi, M., Tanaka, T., Bizen, T., Gote, S., Maréchal, X. M., Seike, T., Tamasaku, K., Ishikawa, T. & Kitamura, H. (2002). *Rev. Sci. Instrum.* **73**, 1125–1128.

Hart, M. & Berman, L. (1998). *Acta Cryst.* A**54**, 850–858, http://dx.doi.org/10.1107/S0108767398011283.

He, H., Marchesini, S., Howells, M., Weierstall, U., Chapman, H., Hau-Riege, S., Noy, A. & Spence, J. C. H. (2003). *Phys. Rev. B*, **67**, 174114.

He, H., Marchesini, S., Howells, M., Weierstall, U., Hembree, G. & Spence, J. C. H. (2003). *Acta Cryst.* A**59**, 143–152.

Helliwell, J. R. (1998). *Acta Cryst.* A**54**, 738–749.

Hignette, O., Cloetens, P., Rostaing, G., Bernard, P. & Morawe, C. (2005). *Rev. Sci. Instrum.* **76**, 063709.

Hignette, O., Rostaing, G., Cloetens, P., Ludwig, A. R. & Freund, A. (2001). *Proc. SPIE*, **4499**, 105–116.

Hohenberg, P. C. & Halperin, B. I. (1977). *Rev. Mod. Phys.* **49**, 436–479.

Howells, M. R., Beetz, T., Chapman, H. N., Cui, C., Holton, J. M., Jacobsen, C. J., Lima, J. K. E., Marchesini, S., Miao, H., Sayre, D., Shapiro, D. A. & Spence, J. C. H. (2005). *J. Electron Spectrosc. Rel. Phenom.*, http://www.citebase.org/abstract?id=oai%3AarXiv.org%3Aphysics%2F0502059.

Kim, H. Y., Ruhm, A., Lurio, L. B., Basu, J. K., Lal, J., Mochrie, S. G. J. & Sinha, S. K. (2004). *J. Phys. Condens. Matter*, **16**, S3491–S3497.

Kohmura, Y., Nishino, Y., Ishikawa, T. & Miao, J. (2005). *J. Appl. Phys.* **98**, 123105.

Krall, A. H. & Weitz, D. A. (1998). *Phys. Rev. Lett.* **80**, 778–781.

Lal, J., Abernathy, D., Auvray, L., DSiat, O. & Grübel, G. (2001). *Eur. Phys. J.* **E4**, 263–271.

Le Bolloc'h, D., Livet, F., Bley, F., Schulli, T., Véron, M. & Metzger, T. H. (2002). *J. Synchrotron Rad.* **9**, 258–265.

Le Bolloc'h, D., Ravy, S., Dumas, J., Marcus, J., Livet, F., Detlefs, C., Yakhou, F. & Paolasini, L. (2005). *Phys. Rev. Lett.* **95**, 116401.

Leitenberger, W., Wendrock, H., Bischoff, L., Panzner, T., Pietsch, U., Grenzer, J. & Pucher, A. (2003). *Physica (Uttrecht)*, B**336**, 63–67.

Lengeler, B. (2001). *Naturwissenschaften*, **88**, 249–260.

Lengeler, B., Schroer, C., Tümmler, J., Benner, B., Richwin, M., Snigirev, A. Snigireva, I. & Drakopoulos, M. (1999). *J. Synchrotron Rad.* **6**, 1153–1167.

Lengeler, B., Schroer, C. G., Benner, B., Gerhardus, A., Günzler, T. F., Kuhlmann, M., Meyer, J. & Zimprich, C. (2002). *J. Synchrotron Rad.* **9**, 119–124.

Lengeler, B., Schroer, C. G., Kuhlmann, M., Benner, B., Günzler, T. F., Kurapova, O., Zontone, F., Snigirev, A. & Snigireva, I. (2005). *J. Phys. D Appl. Phys.* **38**, A218–A222.

Lengeler, B., Tümmler, J., Snigirev, A., Snigireva, I. & Raven, C. (1998). *J. Appl. Phys.* **84**, 5855–5861.

Létoublon, A., Yakhou, F., Livet, F., Bley, F., de Boissieu, M., Mancini, L., Vettier, C. & Gastaldii, J. (2001). *Europhys. Lett.* **54**, 753–759.

Li, C. H., Koga, T., Jiang, J., Sharma, S., Narayanan, S., Lurio, L. B., Hu, Y., Jiao, X., Sinha, S. K., Billet, S., Sosnowik, D., Kim, H., Sokolov, J. C. & Rafailovich, M. H. (2005). *Macromolecules*, **38**, 5144–5151.

Lifshitz, I. M. & Slyozov, V. V. (1961). *J. Phys. Chem. Solids*, **19**, 35.

Liu, C., Conley, R., Macrander, A. T., Graber, T. J., Morawe, C., Borel, C. & Dufresne, E. M. (2004). *Proc. SPIE*, **5537**, 154–160.

Livet, F., Bley, F., Caudron, R., Geissler, E., Abernathy, D., Detlefs, C., Grübel, G. & Sutton, M. (2001). *Phys. Rev. E*, **63**, 036108.

Livet, F., Bley, F., Ehrburger-Dolle, F., Geissler, E., Le Bolloc'h, D. & Schulli, T. (2003). *J. Appl. Cryst.* **36**, 774–777.

Livet, F., Bley, F., Létoublon, A., Simon, J. P. & Bérar, J. F. (1998). *J. Synchrotron Rad.* **5**, 1337–1345.

Livet, F., Bley, F., Mainville, J., Sutton, M., Mochrie, S., Geissler, E., Dolino, G., Abernathy, D. & Grübel, G. (2000). *Nucl. Instrum. Methods*, A**451**, 596–609.

Livet, F., Bley, F., Morfin, I., Ehrburger-Dolle, F., Geissler, E. & Sutton, M. (2006). *J. Synchrotron Rad.* **13**, 453–458.

Livet, F., Bley, F., Simon, J.-P., Caudron, R., Mainville, J., Sutton, M. & Lebolloc'h, D. (2002). *Phys. Rev. B*, **66**, 134108.

Löcker, M., Fischer, P., Krimmel, S., Krüger, H., Lindner, M., Nakazawa, K., Takahashi, T. & Wermes, N. (2004). *IEEE Trans. Nucl. Sci.* **51-4**, 1717–1723.

Ludwig, K., Livet, F., Bley, F., Simon, J.-P., Caudron, R., Le Bolloc'h, D. & Moussaid, A. (2005). *Phys. Rev. B*, **72**, 144201.

Lumma, D., Lurio, L. B., Borthwick, M. A., Falus, P. & Mochrie, S. G. J. (2000). *Phys. Rev. E*, **62**, 8258–8269.

Lumma, D., Lurio, L. B., Mochrie, S. G. J. & Sutton, M. (2000). *Rev. Sci. Instrum.* **71**, 3274–3284.

Madsen, A., Seydel, T., Sprung, M., Gutt, C., Tolan, M. & Grübel, G. (2004). *Phys. Rev. Lett.* **92**, 096104.

Madsen, A., Seydel, T., Tolan, M. & Grübel, G. (2005). *J. Synchrotron Rad.* **12**, 786–794.

Malik, A., Sandy, A. R., Lurio, L. B., Stephenson, G. B., Mochrie, S. G. J., McNulty, I. & Sutton, M. (1998). *Phys. Rev. Lett.* **81**, 5832–5835.

Marchesini, S., Chapman, H. M., Hau-Riege, S. P., London, R. A., Snoke, A., He, H., Howells, M. R., Padmore, H., Rosen, R.,

Spence, J. H. C. & Weierstall, U. (2003). *Opt. Express*, **11**, 2344–2353.

Marchesini, S., Fezzaa, K., Belakhovsky, M. & Cosson, R. (2000). *Appl. Opt.* **39**, 1633–1636.

Marchesini, S., He, H., Chapman, H. N., Hau-Riege, S. P., Noy, A., Howells, M. R., Weierstall, U. & Spence, J. C. H. (2003). *Phys. Rev. B*, **68**, 140101.

Martynov, V. V., Platonov, Y., Kazimirov, A. & Bilderback, D. H. (2004). *AIP Conf. Proc.* **705**, 697–700.

Menteş, T. O., Sanchez-Hanke, C. & Kao, C. C. (2002). *J. Synchrotron Rad.* **9**, 90–95.

Miao, J., Charalambous, P., Kirz, J. & Sayre, D. (1999). *Nature (London)*, **400**, 342–344.

Miao, J., Ishikawa, T., Johnson, B., Anderson, E. H., Lai, B. & Hodgson, K. O. (2002). *Phys. Rev. Lett.* **89**, 08303.

Miao, J., Sayre, D. & Chapman, H. N. (1998). *J. Opt. Soc. Am.* A**15**, 1662–1669.

Mielenz, K. D. (1999). *J. Res. Natl Inst. Stand. Technol.* **104**, 479–485.

Millane, R. P. (1996). *J. Opt. Soc. Am.* A**13**, 725–734.

Mochrie, S. G. J., Lurio, L. B., Ruhm, A., Lumma, D., Borthwick, M., Falus, P., Kim, H. J., Basu, J. K., Lal, J. & Sinha, S. K. (2003). *Physica (Uttrecht)*, B**336**, 173–180.

Mochrie, S. G. J., Mayes, A. M., Sandy, A. R., Sutton, M., Brauer, S., Stephenson, G. B., Abernathy, D. L. & Grübel, G. (1997). *Phys. Rev. Lett.* **78**, 1275–1279.

Morawe, C., Peffen, J.-C., Ziegler, E. & Freund, A. K. (2003). *Proceedings of SPIE*, **4145**, 61–71.

Nikulin, A. Y. & Davis, J. R. (1988). *Opt. Commun.* **155**, 231–235.

Nöhammer, B., Hoszowska, J., Herzig, H. P. & David, C. (2003). *J. Phys. IV France*, **104**, 193–196.

Panzner, T., Leitenberger, W., Grenzer, J., Bodenthin, Y., Geue, T., Pietsch, U. & Möhwald, H. (2003). *J. Phys. D Appl. Phys.* **36**, A93.

Papagiannopoulos, A., Waigh, T. A., Fluerasu, A., Fernyhough, C. & Madsen, A. (2005). *J. Phys. Condens. Matter*, **17**, L279–L285.

Paterson, D., Allman, B., McMahon, P., Lin, J., Moldovan, N., Nugent, K., McNulty, I., Chantler, C., Retsch, C., Irving, T. & Mancini, D. (2001). *Opt. Commun.* **195**, 79–84.

Petukhov, A. V., Thijssen, J. H. J., 't Hart, D. C., Imhof, A., van Blaaderen, A., Dolbnya, I. P., Snigirev, A., Moussaïd, A. & Snigireva, I. (2006). *J. Appl. Cryst.* **39**, 137–144.

Pfeifer, M. A., Williams, G. J., Vartanyants, I. A., Harder, R. & Robinson, I. K. (2006). *Nature (London)*, **442**, 63–66.

Pfeiffer, F., Bunk, O., Schulze-Briese, C., Diaz, A., Weitkamp, T., David, C., van der Veen, J. F., Vartanyants, I. & Robinson, I. K. (2005). *Phys. Rev. Lett.* **94**, 164801.

Pfeiffer, K.-F., Giersch, J. & Anton, G. (2004). *Nucl. Instrum. Methods*, A**531**, 246–250.

Pfeiffer, K.-F. G., Giersch, J., Anton, G., Bätz, L. & Hoheisel, M. (2003). *Nucl. Instrum. Methods*, A**509**, 340–345.

Pietsch, U., Panzner, T., Leitenberger, W. & Vartanyans, I. (2005). *Physica (Utrecht)*, B**357**, 45–52.

Pitney, J. A., Robinson, I. K., Vartanyans, I. A., Appelton, R. & Flynn, C. P. (2000). *Phys. Rev. B*, **62**, 13084–13088.

Platonov, Y. Y., Martynov, V. V., Kazimirov, A. & Lai, B. (2004). *Proc. SPIE*, **5537**, 161–170.

Price, A. C., Sorensen, L. B., Kevan, S. D., Toner, J., Poniewierski, A. & Holyst, R. (1999). *Phys. Rev. Lett.* **82**, 755–758.

Retsch, C. C., McNulty, I. & Iannacchione, C. S. (2002). *Phys. Rev. E*, **65**, 032701.

Riese, D. O., Wegdam, G. H., Vos, W. L., Sprik, R., Fenistein, D., Bongaerts, J. H. H. & Grübel, G. (2000). *Phys. Rev. Lett.* **85**, 5460–5463.

Robert, A., Wagner, J., Autenrieth, T., Hartl, W. & Grübel, G. (2005). *J. Magn. Magn. Mater.* **289**, 47–49.

Robinson, I., Pfeiffer, F., Vartanyants, I. A., Sun, Y. & Xia, Y. (2003). *Opt. Express*, **11**, 2329–2334.

Robinson, I. K. & Miao, J. (2004). *MRS Bull.* **29**, 177–181.

Robinson, I. K. & Vartanyans, I. A. (2001). *Surf. Appl. Sci.* **182**, 186–191.

Robinson, I. K., Vartanyants, I. A., Williams, G. J., Pfeifer, M. A. & Pitney, J. A. (2001). *Phys. Rev. Lett.* **87**, 195505.

Rossi, G., Renzi, M., Eikenberry, E. F., Tate, M. W., Bilderback, D., Fontes, E., Wixted, R. & Gruner, S. M. (1999). *J. Synchrotron Rad.* **6**, 1096–1105.

Sandy, A. R., Lurio, L. B., Mochrie, S. G. J., Malik, A., Stephenson, G. B., Pelletier, J. F. & Sutton, M. (1999). *J. Synchrotron Rad.* **6**, 1174–1184.

Sayre, D., Chapman, H. N. & Miao, J. (1998). *Acta Cryst.* A**54**, 232–239.

Scheffold, F. & Schurtenberger, P. (2003). *Soft Mater.* **1**, 139–165.

Schroer, C. G., Kuhlmann, M., Hunger, U. T., Günzler, T. F., Kurapova, O., Feste, S., Frehse, F., Lengeler, B., Drakopoulos, M., Somogyi, A., Simionovici, A. S., Snigirev, A., Snigireva, I., Schug, C. & Schröder, W. H. (2003). *Appl. Phys. Lett.* **82**, 1485–1487.

Seydel, T., Madsen, A., Tolan, M., Grubel, G. & Press, W. (2001). *Phys. Rev.* **63**, 073409.

Shechtman, D., Blech, I., Gratias, D. & Cahn, J. W. (1984). *Phys. Rev. Lett.* **53**, 1951–1953.

Shen, Q., Bazarov, I. & Thibaud, P. (2004). *J. Synchrotron Rad.* **11**, 432–438.

Sikharulidze, I., Dolbnya, I. P., Fera, A., Madsen, A., Ostrovskii, B. I. & de Jeu, W. H. (2002). *Phys. Rev. Lett.* **88**, 115503.

Sikharulidze, I., Dolbnya, I. P., Madsen, A. & de Jeu, W. H. (2005). *Opt. Commun.* **247**, 111–124.

Sikharulidze, I., Farago, B., Dolbnya, I. P., Madsen, A. & de Jeu, W. H. (2003). *Phys. Rev. Lett.* **91**, 165504.

Sikharulidze, I. & de Jeu, W. H. (2005). *Phys. Rev.* **72**, 011704.

Snigirev, A., Kohn, V., Snigireva, I. & Lengeler, B. (1996). *Nature (London)*, **384**, 49–51.

Stadler, L. M., Sepiol, B., Kantelhardt, J. W., Zizak, I., Grübel, G. & Vogl, G. (2004). *Phys. Rev. B*, **69**, 224301.

Stadler, L. M., Sepiol, B., Pfau, B., Vogl, G. & Zontone, F. (2005). *Nucl. Instrum. Methods*, B**238**, 189–191.

Stadler, L. M., Sepiol, B., Weinkamer, R., Hartmann, M., Fratzl, P., Kantelhardt, J. W., Zontone, F., Grübel, G. & Vogl, G. (2003). *Phys. Rev.* **68**, 180101.

Sutton, M., Laaziri, K., Livet, F. & Bley, F. (2003). *Opt. Express*, **11**, 2268–2277.

Sutton, M., Li, Y., Brock, J. D. & Thorne, R. E. (2002). *J. Phys. IV France*, **12**, 3–8.

Sutton, M., Mochrie, S. G. J., Greytak, T., Nagler, S. E., Berman, L. E., Held, G. E. & Stephenson, G. B. (1991). *Nature (London)*, **352**, 608–610.

Suzuki, Y., Momose, A. & Sugiyama, H. (1998). *J. Synchrotron Rad.* **5**, 596–599.

Thurn-Albrecht, T., Meier, G., Müller-Buschbaum, P., Patkowski, A., Steffen, W., Grübel, G., Abernathy, D. L., Diat, O., Winter, M., Koch, M. G. & Reetz, M. T. (1999). *Phys. Rev.* **59**, 642–647.

Thurn-Albrecht, T., Steffen, W., Meier, A. P. G., Fischer, E., Grübel, G. & Abernathy, D. L. (1996). *Phys. Rev. Lett.* **77**, 5437–5440.

Thurn-Albrecht, T., Zontone, F., Grübel, G., Steffen, W., Müller-Buschbaum, P. & Patkowski, A. (2003). *Phys. Rev. E*, **68**, 031407.

Toellner, T. S., Hu, M. Y., Sturhahn, W., Bortel, G., Alp, E. E. & Zhao, J. (2001). *J. Synchrotron Rad.* **8**, 1082–1086.

Tran, C. Q., Peele, A. G., Paterson, D., Roberts, A., McNulty, I. & Nugent, K. A. (2005). *J. Electron Microsc. Relat. Phenom.* **114**, 947–951.

Tsui, O. K. C., Mochrie, S. G. J. & Berman, L. E. (1998). *J. Synchrotron Rad.* **5**, 30–36.

Uhlenbeck, G. E. & Ornstein, L. S. (1930). *Phys. Rev.* **36**, 823–841.

Vartanyants, I. A. & Robinson, I. K. (2001). *J. Phys. Condens. Matter*, **13**, 10593–10611.

Veen, F. van der & Pfeiffer, F. (2004). *J. Phys. Condens. Matter*, **16**, 5003–5030.

Verbeni, R., Sette, F., Krisch, M. H., Bergmann, U., Gorges, B., Halcoussis, C., Martel, K., Masciovecchio, C., Ribois, J. F., Ruocco, G. & Sinn, H. (1996). *J. Synchrotron Rad.* **3**, 62–64.

Vlieg, E., Vries, S. A. D., Alvarez, J. & Ferrer, S. (1997). *J. Synchrotron Rad.* **4**, 210–213.

Wagner, C. (1961). *Z. Elektrochem.* **65**, 581.

Wagner, J., Autenrieth, T., Robert, A., Hartl, W. & Grübel, G. (2005). *J. Magn. Magn. Mater.* **289**, 54–57.

Weinkamer, R. & Fratzl, P. (2003). *Europhys. Lett.* **61**, 261–267.

Wiedenmann, A. & Heinemann, A. (2005). *J. Magn. Magn. Mater.* **289**, 58–61.

Williams, G. J., Pfeifer, M. A., Vartanyants, I. A. & Robinson, I. K. (2003). *Phys. Rev. Lett.* **90**, 175501.

Williams, G. J., Pfeifer, M. A., Vartanyants, I. A. & Robinson, I. K. (2006). *Phys. Rev. B*, **73**, 094112.

Yabashia, M., Mochizuki, T., Yamazaki, H., Goto, S., Ohashi, H., Takeshita, K., Ohata, T., Matsushita, T., Tamasaku, K., Tanaka, Y. & Ishikawa, T. (2001). *Nucl. Instrum. Methods*, **467–468**, 678–681.

Yamamura, K., Yamauchi, K., Mimura, H., Sano, Y., Saito, A., Endo, K., Souvorov, A., Yabashi, M., Tamasaku, K., Ishikawa, T. & Mori, Y. (2003). *Rev. Sci. Instrum.* **74**, 4549–4553.

Yamauchi, K., Yamamura, K., Mimura, H., Sano, Y., Saito, A., Souvorov, A., Yabashi, M., Tamasaku, K., Ishikawa, T. & Mori, Y. (2002). *J. Synchrotron Rad.* **9**, 313–316.

Yun, W., Lai, B., Cal, Z., Maser, J., Legnini, D., Gluskin, E., Chen, Z., Krasnoperova, A. A., Vladimirski, Y., Cerrina, F., Fabrizio, E. D. & Gentili, M. (1999). *Rev. Sci. Instrum.* **70**, 2238–2241.

Ziegler, E., Hignette, O., Morawe, C. & Tucoulou, R. (2001). *Nucl. Instrum. Methods*, A**467–468**, 954–957.

Zorzia, N., Bisogni, M., Boscardin, M., Betta, G.-F. D., Gregori, P., Novelli, M., Piemonte, C., Quattrocchi, M., Ronchin, S. & Rosso, V. (2005). *Nucl. Instrum. Methods*, A**546**, 46–50.